



Near-surface mercury vapour haloes in air above ore deposits and faults on Vancouver Island: Insights into buried materials in real-time?

Alexei S. Rukhlov^{1, a}, Luke Ootes¹, Adrian S. Hickin¹, and Nikolay R. Mashyanov²

¹ British Columbia Geological Survey, Ministry of Energy, Mines and Low Carbon Innovation, Victoria, BC, V8W 9N3

² Lumex-marketing LLC, 1 lit. B, Obruchevykh Street, St. Petersburg, 195220, Russia

^a corresponding author: Alexei.Rukhlov@gov.bc.ca

Recommended citation: Rukhlov, A.S., Ootes, L., Hickin, A.S., and Mashyanov, N.R., 2021. Near-surface mercury vapour haloes in air above ore deposits and faults on Vancouver Island: Insights into buried materials in real-time? In: *Geological Fieldwork 2020*, British Columbia Ministry of Energy, Mines and Low Carbon Innovation, British Columbia Geological Survey Paper 2021-01, pp. 113-143.

Abstract

Volatile geogenic components, such as CO₂, He, Rn, and Hg, form haloes in soil gas and near-surface air directly above mineral deposits. This contrasts with lithochemical, hydrochemical, and biochemical dispersion haloes that can be laterally displaced or obscured by transported overburden. Mercury vapour surveys have been used in geochemical exploration, because Hg occurs in most types of endogenic ore deposits and is highly mobile. In this study, we measured Hg vapour in air 1-50 cm above ground at 15 sites on Vancouver Island. To evaluate the effectiveness of the method across a range of settings, these sites include different types of known mineralized zones, barren rocks, and faults, both buried and exposed. The direct and continuous analysis via a portable RA-915M mercury analyzer reveals Hg vapour concentrations ranging from 0.5 to 54.4 ng·m⁻³. The highest Hg concentration was observed above tailings at the Bentley Au occurrence, possibly due to the amalgamation technique used for fine gold extraction between late 1800s and early 1900s. Prominent Hg vapour haloes mark shear-hosted Cu-Ag-Au sulphides at Mount Skirt (13.4x background Hg), epithermal Au-Ag-Cu at Mount Washington (8.9x background Hg), and sediment-covered polymetallic volcanogenic massive sulphide at the Lara-Coronation occurrence (4.2 to 6.6x background Hg). Basalt-hosted Cu-Ag-Au sulphide zones at the Sunro past producer are marked by weak Hg vapour anomalies relative to local background. Faults, including the Leech River fault, which was active in the Quaternary, are also marked by weak Hg vapour anomalies. The study confirms that, although the Hg level is influenced by weather, the real-time Hg vapour measurement of near-surface air can instantly delineate mineralized zones and fault structures that are buried under overburden 10s of m thick. In contrast to soil gas sampling, this simple and rapid technique can be applied to mineral exploration and geological mapping under overburden above any type of surface, including outcrops, talus, bogs, water bodies, snow, and permafrost.

Keywords: Mercury vapour haloes, near-surface air, real-time analysis, portable RA-915M mercury analyzer, overburden, Leech River fault, Vancouver Island, mineral exploration under cover, polymetallic volcanogenic massive sulphide, epithermal Au-Ag-Cu, shear-hosted sulphide Cu-Ag-Au, Lara-Coronation, Mount Washington Copper, Sunro, Bentley Au, Ralph

1. Introduction

Volatile geogenic components, such as CO₂, SO₂, He, Rn, and Hg, form haloes in soil gas and near-surface atmosphere directly above ore and oil and gas deposits and fault zones (e.g., Sokolov, 1956; Williston, 1968; Ovchinnikov et al., 1972; Fridman, 1975; Mashyanov, 1993; Wang et al., 2006; Utkin and Yurkov, 2010; Kalinchuk and Astakhov, 2014; Sun et al., 2017; Buttitta et al., 2020; Esbril et al., 2020; Lett et al., 2020; Xiang et al., 2020). This contrasts with lithochemical, hydrochemical, and biochemical dispersion aureoles that can be laterally displaced or obscured by transported overburden (Solovov, 1985). Because volatile geogenic species are highly mobile, they migrate to the surface from deep sources such as blind and buried ore deposits and thus form superimposed dispersion haloes.

Among atmospheric methods, Hg vapour surveys have been most useful in exploration (e.g., Sergeev, 1957; Hawkes and Williston, 1962; Fursov, 1990), geological mapping (e.g., Xiang et al., 2020), and earthquake prediction (e.g., Jin et al.,

1989; Wang et al., 2006). This is because Hg occurs in many hydrothermal ore deposit types, is highly mobile, and forms vapour haloes in soil gas and atmosphere above ore and oil and gas deposits, active faults, volcanoes, and geothermal zones (e.g., Fursov, 1970, 1983, 1990; McCarthy, 1972; Ozerova, 1975, 1986; Nriagu and Becker, 2003; Kalinchuk and Astakhov, 2014; Sun et al., 2017). Low background concentrations in the atmosphere (1.2 to 1.5 ng·m⁻³; Sprovieri et al., 2016) enable detecting even weak Hg emissions directly above buried ore deposits 100s of m below the surface (e.g., Krömer et al., 1981; Zonghua and Yangfen, 1981; Fursov, 1990; Zherebtsov et al., 1992; Rehn and Rehn, 1996).

In the present study, we evaluate the effectiveness of real-time Hg vapour measurement in air 1-50 cm above ground at 15 locations on Vancouver Island. These sites include different types of sediment-covered and exposed mineralized zones and faults. We use a direct and continuous analysis of ultra-low Hg concentrations in air via a portable RA-915M mercury analyzer that has a response time of one second and a detection range of

0.5-20,000 ng·m⁻³ (Sholupov et al., 2004). Our study finds that a simple, real-time Hg vapour sampling of near-surface air can instantly delineate mineralized zones and faults that are buried under overburden 10s of m thick.

2. Geochemistry of mercury

2.1. Mercury as an indicator of endogenic processes and ore deposits

Mercury is the only metal that forms vapour haloes in soil gas and near-surface atmosphere that currently can be directly detected. Mercury readily reduces to chemically stable Hg⁰, which is highly volatile, actively evaporates, adsorbs, and dissolves other metals (Smirnov, 1955; Sveshnikov, 1967; Kothny, 1973; Fursov, 1983b; Schuster, 1991; Zhang and Lindberg, 1999; Gu et al., 2011; Moore and Castro, 2012). Mercury forms more than 30 minerals, including native mercury and amalgams, and concentrates in low-temperature hydrothermal minerals such as pyrite (up to 6%), tennantite-tetrahedrite (up to 21.9%), and sphalerite (up to 35%; Saukov et al., 1972). High mobility and the association with most ore deposit types make Hg vapour an ideal indicator of endogenic ore deposits and tectonic, geothermal, and volcanic activity (Kuznetsov and Obolensky, 1970; Ozerova, 1975, 1976, 1977, 1979, 1986; Babkin et al., 1976; Fursov, 1977, 1983b; Fedorchuk, 1983; Carr et al., 1984; Stepanov, 1997; Stoffers et al., 1999; Nriagu and Becker, 2003; Ryzhov et al., 2003; Rychagov et al., 2009; Yin et al., 2020).

Predicted by A.A. Saukov, ‘mercury atmosphere’ of ore deposits is the basis of Hg vapour exploration method (Saukov, 1946; Saukov et al., 1972). Along with the development of technology for direct analysis, Hg vapour surveys have been increasingly applied in exploration (Sergeev, 1957; Hawkes and Williston, 1962; Fedorchuk, 1964; Barringer, 1966, 1969; McCarthy et al., 1969, 1970; McCarthy, 1972; Fursov, 1970, 1983a, 1990; Karasik et al., 1978; Mashyanov, 1980, 1985; Krömer et al., 1981; Zonghua and Yangfen, 1981; Chengliang et al., 1989; Zherebtsov et al., 1992; Rehn and Rehn, 1996; Yasutake et al., 2011; Higuera et al., 2012; Bradshaw, 2015; Nevolko and Fominykh, 2017). Low global background in atmosphere (1.2 to 1.5 ng·m⁻³; Sprovieri et al., 2016) reflects low lithospheric background (45 ppb Hg; Rudnick and Gao, 2005) and enables detecting even weak Hg haloes of ore deposits and emanations through fault zones (Ozerova, 1977; Mashyanov, 1980, 1985; Jin et al., 1989; Wang et al., 2006; Kalinchuk and Astakhov, 2014; Sun et al., 2017; Xiang et al., 2020).

2.2. Mercury emission into the atmosphere

The global distribution of Hg in belts such as the Cordilleran orogen, which hosts more than 1,500 occurrences (e.g., Pinchi Lake ore field, British Columbia) reflects migration of Hg from the mantle along deep, linear structures (Fedorchuk, 1964, 1983; Kuznetsov and Obolenskiy, 1970; Ozerova, 1976, 1977, 1986). Some oil and gas pools in these belts have Hg resources comparable to those of Hg mines (Ozerova, 1975, 1976;

Mashyanov, 1985; Ryzhov et al., 2003). Mercury migrates to the surface mostly as Hg⁰ vapour due to tectonic, hydrothermal, and volcanic activity (Saukov et al., 1972; Ozerova, 1977). Anomalous Hg emissions, including formation of modern Hg deposits, mark mantle plumes (e.g., Hawaii and Iceland), mid-ocean ridges, volcanic arcs, geothermal fields, and active faults (Boström and Fischer, 1969; Eshleman et al., 1971; Aston et al., 1972; Carr et al., 1974, 1975; Coderre and Steinthorsson, 1977; Ozerova, 1977; Jin et al., 1989; Stepanov, 1997; Stoffers et al., 1999; Nriagu and Becker, 2003; Rychagov et al., 2009; Kalinchuk and Astakhov, 2014). Processes such as fuel combustion (mainly coal) and artisanal gold mining are the most significant anthropogenic sources of Hg emissions into atmosphere (Higuera et al., 2012; Dalziel and Tordon, 2014; Gworek et al., 2017; Mashyanov et al., 2017; UN Environment, 2019). Elemental mercury (Hg⁰) vapour comprises more than 95% of the atmospheric Hg species (Sprovieri et al., 2016). Generally consistent atmospheric background can be influenced by local meteorological factors such as precipitation of Hg adsorbed on aerosols and shows significant seasonal variations (Williston, 1968; McCarthy et al., 1970; Krömer et al., 1981; Mashyanov, 1985; Dalziel and Tordon, 2014; Bradshaw, 2015).

2.3. On the origin of Hg vapour haloes in soil gas and near-surface air

Mercury emitted into atmosphere is diluted by turbulent diffusion and transferred with air mass movement. Hence, Hg vapour haloes (up to $n \cdot 10^3 \times$ background Hg) occur in soil gas and near-surface atmosphere directly above ore deposits rather than forming dispersal plumes (Sergeev, 1957; McCarthy et al., 1969, 1970; Fursov, 1970, 1983a, 1990; Krömer et al., 1981; Mashyanov, 1985; Zherebtsov et al., 1992). Processes that generate Hg vapour haloes include: 1) upward diffusion-filtration of Hg along permeable zones due to the temperature, pressure, and concentration gradients, coupled with the chemical stability and high mobility of Hg⁰ (e.g., Ozerova, 1977); 2) sublimation of Hg⁰ from Hg-bearing minerals (e.g., Smirnov, 1955; Fursov, 1983a); 3) reduction of Hg²⁺ to Hg⁰ with CO₂, H₂, and CH₄ in the supergene zone (e.g., Saukov, 1946; Mashyanov, 1980, 1985); 4) ionic and cathode electrochemical reactions within ore bodies and enclosing strata (e.g., Sveshnikov, 1967; Mashyanov et al., 1995); 5) oxidation of Hg-bearing sulphides by plants and bacteria and Hg vapour transpiration from plants (e.g., Barringer, 1969; Gu et al., 2011; Bradshaw, 2015).

Soil temperature, moisture, redox potential, permeability, and organic matter are important factors that influence Hg vapour concentration in soil gas (McCarthy, 1972; Chengliang et al., 1989; Schuster, 1991; Zhang and Lindberg, 1999; Choi and Holsen, 2009; Gu et al., 2011; Yasutake et al., 2011; Higuera et al., 2012; Moore and Castro, 2012; Xie et al., 2019; Esbril et al., 2020). Chengliang et al. (1989) suggest that Hg in overburden (up to 40 m thick) over the blind Fankou Pb-Zn deposit (>200 m below the surface) in Guangdong (China) occurs mainly as free vapour and adsorbed onto soil colloids such as clays and Fe-Mn oxides. Mercury vapour haloes in soil gas are up to 40x

background Hg above the deposit (Chengliang et al., 1989). Theoretical modelling of overburden thickness and sorption and diffusion processes shows that the intensity of Hg vapour anomalies in near surface air decreases exponentially with increasing overburden thickness (Mashyanov, 1980, 1985; Sun et al., 2017). Mercury vapour anomalies in soil gas above a skarn Cu deposit buried under alluvium (up to 180 m thick) near Shanghai (China) had similar shape and intensity between the repeated surveys carried out in different seasons (Zonghua and Yangfen, 1981).

2.4. Soil gas sampling versus near-surface air sampling

Because of higher Hg vapour concentration (Fursov, 1990; Zherebtsov et al., 1992), soil gas sampling is more commonly used than near-surface air sampling (Mashyanov, 1980; Krömer et al., 1981; Yasutake et al., 2011). However, soil gas sampling is not suitable across highly variable surficial materials, outcrops, talus, wet soil, bogs, water bodies, permafrost, and snow cover (McCarthy, 1972; Mashyanov, 1985). It is also slower compared to real-time sampling of air above ground which is as rapid as a geophysical survey. In addition, Hg analyzers using gold traps to pre-concentrate Hg from soil gas have variable sample conditions depending on composition and porosity of the surficial materials. Furthermore, soil moisture strongly impacts sorption ability of the gold trap, creating concentration readings bias (Mashyanov, 1985; Zherebtsov et al., 1992). Moreover, Hg vapour concentration in soil gas strongly depends on the time lapse between the borehole drilling and measurement, speed of drilling, depth of borehole, and sampler shape (Zherebtsov et al., 1992; Stepanov, 1997; Sun et al., 2017). In contrast, the near-surface air measurement is free of such sampling conditions and can be more efficient (Mashyanov, 1980, 1985; Yasutake et al., 2011).

3. Geological setting, Vancouver Island

Vancouver Island is mainly underlain by Late Paleozoic to Early Mesozoic rocks of Wrangell terrane, with slivers of Pacific Rim and Crescent terranes along the west coast and southern tip of the island (Fig. 1; Muller, 1977; Nelson et al., 2013). Amalgamated with Alexander terrane by the Late Carboniferous, Wrangellia, now part of the Insular superterrane, accreted to inboard Intermontane terranes between Middle Jurassic and mid-Cretaceous (Nelson et al., 2013).

The oldest rocks of Wrangellia on Vancouver Island comprise volcanic and volcanoclastic strata of the Sicker Group (Middle to Late Devonian) and coeval felsic intrusions of the Saltspring plutonic suite, which record the evolution of an oceanic island arc. Intermediate to felsic volcanic rocks of the Sicker Group host significant volcanogenic massive sulphide (VMS) mineralization (e.g., Lara-Coronation, MINFILE 092B 129; Northcote and Muller, 1972; Muller, 1977; Massey, 1995; Yorath, 2005; Kelso and Wetherup, 2008; Ruks, 2015). Epiclastic sedimentary rocks and bioclastic limestone of the Buttle Lake Group (Mississippian to Early Permian) overlie the arc strata. Folded and imbricated by thrust faults, rocks of

the Sicker and Buttle Lake groups are exposed within several northwest-trending uplifts that are the result of the collision of Wrangellia with the North American margin between Middle Jurassic and mid-Cretaceous and subsequent shortening in the Eocene. The Paleozoic rocks are typically metamorphosed to greenschist facies, with amphibolite facies developed near granitoid bodies of the Island plutonic suite (Early to Middle Jurassic).

Much of Vancouver Island is underlain by younger rocks of Vancouver and Bonanza groups. The Vancouver Group (Middle to Late Triassic) consists of flood basalts of the Karmutsen Formation overlain by limestone of the Quatsino Formation. The voluminous flood basalts of the Karmutsen Formation (about 6 km thick), along with coeval mafic intrusions (Mount Hall Gabbro), mark a plume-related, oceanic plateau superimposed on the Paleozoic Sicker arc. Largely subaerial mafic to felsic volcanic and sedimentary strata of the Bonanza Group (Late Triassic to Middle Jurassic) unconformably overlie the older rocks. Together with coeval granitoids of the Island plutonic suite (Early to Middle Jurassic), they record the evolution of the Bonanza magmatic arc that overprinted Wrangellia and brought about major porphyry Cu-Mo-Au and related ore deposits (Carson, 1968; Northcote and Muller, 1972; Muller, 1977; Massey et al., 1994; Yorath, 2005). The Westcoast Crystalline complex (Paleozoic to Jurassic) underlies much of Victoria and consists of metamorphosed and partially melted host rocks that are mixed with Jurassic intrusions.

Cyclic marine and continental sedimentary sequences containing coal beds of the Nanaimo Group (Late Cretaceous) mark deposition in a broad basin along the eastern margin of Wrangellia. Strongly deformed ribbon chert, argillite, phyllite, slate, schists, and metavolcanic rocks of the Leech River (Jurassic to Cretaceous) and Pacific Rim (Triassic to Cretaceous) complexes belong to the Pacific Rim terrane. Juxtaposed against the metamorphic rocks of the Leech River complex along the Leech River fault, basalts and gabbro of the Metchosin Igneous complex (Paleocene to Eocene) underlie the southern tip of Vancouver Island. These rocks make up the Crescent (Siletz in U.S.A.) terrane, which extends more than 650 km south to Oregon and marks the Yellowstone mantle plume-related oceanic plateau accreted to the continental margin between 51 and 45 Ma (e.g., Phillips et al., 2017). The Eocene accretionary events caused folding and faulting of the Nanaimo Group and uplift, resulting in the exposure of metamorphic rocks of the Sicker Group and Westcoast Crystalline complex. The Leech River fault acted as a strike-slip fault during post-Eocene time and was active after the last glacial maximum ca. 17 ka (Morell et al., 2017).

Along the southwestern coast, the older rocks are overlain by a narrow fringe of siliciclastic rocks of the Carmanah Group (Late Eocene to Oligocene). Intermediate and felsic intrusions and related breccia pipes and pyroclastic deposits of the Mount Washington plutonic suite (Eocene to Oligocene) are associated with porphyry Cu-Mo-Au and epithermal Au-Ag-Cu mineralization (Mount Washington

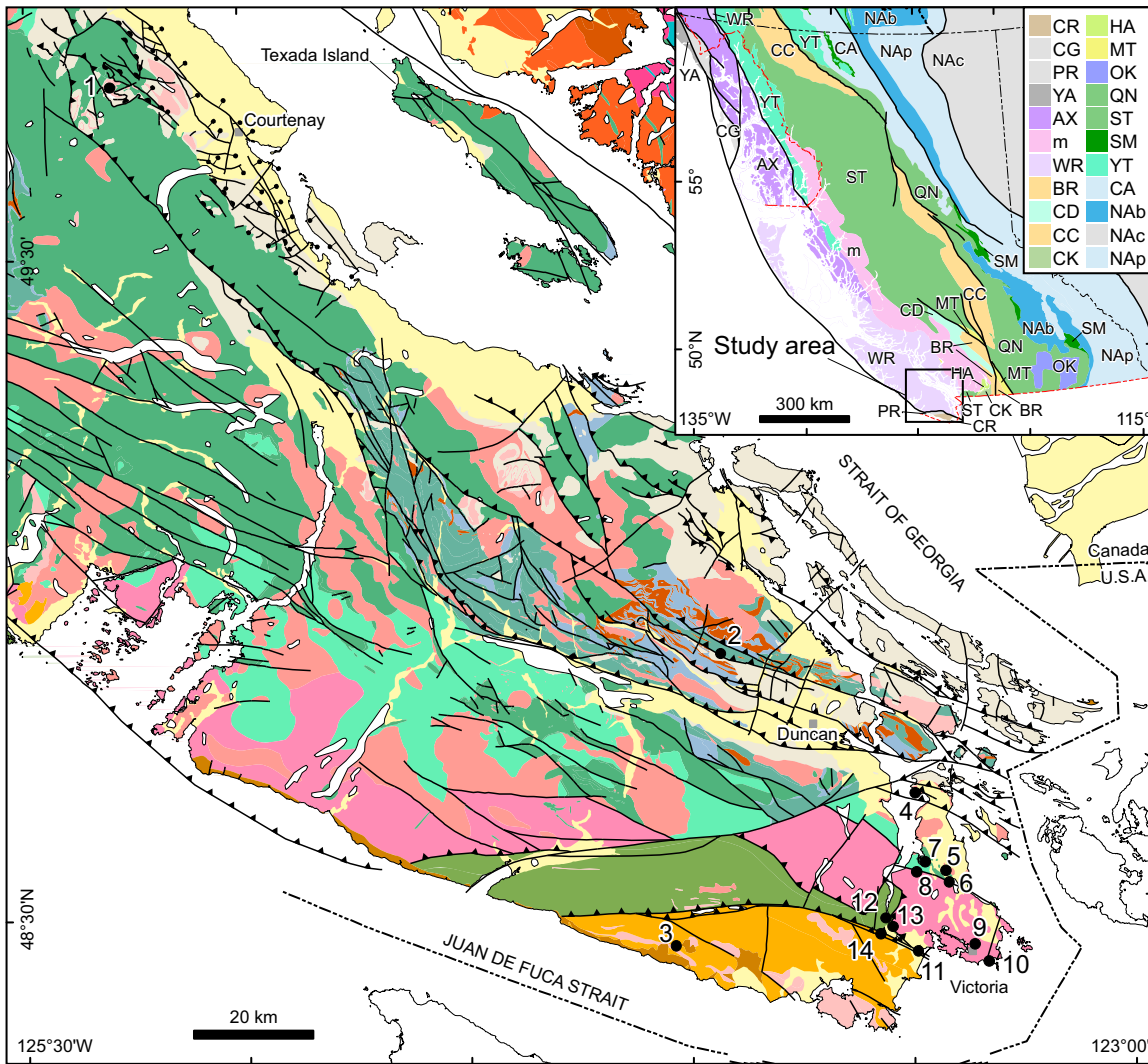


Fig. 1. Survey locations on southern Vancouver Island: 1 – Mount Washington; 2 – Coronation Mountain; 3 – Jordan River; 4 – Deep Cove; 5 – Bear Hill; 6 – Elk Lake; 7 – Tod Inlet; 8 – Durance Lake; 9 – downtown Victoria; 10 – Harling Point; 11 – Colwood; 12 – Goldstream; 13 – Skirt Mountain; and 14 – Sooke Hills. Geology after Cui et al. (2017, 2018) based on Clapp (1912, 1913), Erich and Blanshard (1921), Carson (1960a, b, 1968), Stevenson (1967), Guelpa and Meusy (1971), Meusy (1971), Northcote and Muller (1972), Muller (1977, 1980, 1983, 1989), Clague et al. (1982), Massey et al. (1991, 1994), Massey (1995), Wetherup (2010), Ruks (2015), and Bodnar (2017). Terrane geology after Nelson et al. (2013): Outboard terranes: CR – Crescent, CG – Chugach, PR – Pacific Rim, YA – Yakutat, WR – Wrangellia, m – Coast complex; Intermountain terranes: BR – Bridge River, CD – Cadwallader, CC – Cache Creek, CK – Chilliwack, HA – Harrison Lake, MT – Methow, OK – Okanagan, QN – Quesnellia, ST – Stikinia, SM – Slide Mountain, YT – Yukon-Tanana; Ancestral North American terranes: CA – Cassiar, NAb – Kootenay, NAp – North American platform, NAc – North American craton and cover.

Copper, MINFILE 092F 117; Domineer-Lakeview, MINFILE 092F 116). Auriferous quartz veins hosted by metamorphic rocks of the Leech River complex (Bentley Au, MINFILE 092B 067) and shear-hosted sulphide Cu-Ag-Au (Sunro, MINFILE 092C 073; Ralph, MINFILE 092B 014) also occur on southern Vancouver Island (Carson, 1960a, b, 1968; Northcote and Muller, 1972; Muller, 1977, 1989; Yorath, 2005). Most of the surficial deposits on Vancouver Island formed during or after the Fraser glaciation (Late Wisconsin; Muller, 1977; Clague et al., 1982; Yorath, 2005).

4. Methods

Real-time mercury vapour (Hg^0) mass concentrations (in $\text{ng}\cdot\text{m}^{-3}$) in near-surface atmosphere (i.e. the layer of air 1-50 cm above ground) and simultaneously measured meteorological conditions were acquired during foot traversing at 15 locations on southern Vancouver Island (Fig. 1). Mercury vapour concentration in air was directly and continuously measured via a portable RA-915M differential Zeeman mercury atomic absorption spectrometer using high-frequency modulated light polarization (ZAAS-HFM; Lumex, St. Petersburg, Russia; Sholupov and Ganeyev, 1995; Sholupov et al., 2004). The instrument has a concentration detection range of 0.5 to 20,000 $\text{ng}\cdot\text{m}^{-3}$, a response time of one second, and an analyzed air flow of 10 $\text{L}\cdot\text{m}^{-1}$. Automatic baseline correction using a built-in, high-efficiency (>98%) sorption filter was performed every 10 minutes. Both drift and the standard deviation of zero readings are less than 2 $\text{ng}\cdot\text{m}^{-3}$. The relative intrinsic error of the measurement is less than $\pm 20\%$. Mercury vapour concentrations were automatically normalized to standard temperature (20°C) and pressure (101.3 kPa). We used the average of ten consecutive readings (1 second each), which were automatically stored in the analyzer's memory. Near-surface air was analyzed for at least 20-30 seconds at each stop every 2 to 50 m along a traverse. Air was sampled 10-50 cm above ground directly through instrument's air intake inlet with a built-in dust filter, or 1-10 cm above ground via a 0.5 m long hose (20 mm diameter) attached to the air intake inlet (Fig. 2).

Meteorological parameters such as air temperature, relative humidity, absolute atmospheric (station) pressure, wind speed, and wind direction (azimuth) were simultaneously measured every 5 seconds using a Kestrel 5500 weather meter mounted on a tripod (Fig. 2). We used Garmin Glo 2 GPS-GLONASS and Garmin GPSMap 62sc receivers to acquire coordinates every 5 seconds. Relative pressure (P_0) adjusted to sea-level (in hectopascal, hPa) was calculated according to the World Meteorological Organization's barometric formula from the absolute pressure (P), air temperature (T), and elevation above sea level (h):

$$P_0 = P \cdot (1 - 0.0065h / [T + 0.0065h + 273.15])^{-5.257} \quad (\text{Eqn. 1})$$

where elevation (h) for each data point is interpolated from the British Columbia Terrain Resource Information Mapping (TRIM) digital elevation model using GPS coordinates. Mercury vapour values of $< 0.5 \text{ ng}\cdot\text{m}^{-3}$ (total 156 values or 1.6% of all data) due to abnormal baseline noise were discarded.



Fig. 2. Simultaneous measurement of meteorological conditions and Hg vapour concentrations in near-surface air at Harling Point, southern Vancouver Island.

5. Results

Below we summarize the results of our surveys; the complete dataset is presented in Rukhlov et al. (2020). Mercury vapour survey locations include a variety of known metallic mineral occurrences, barren rocks, and faults on southern Vancouver Island (Fig. 1). Table 1 provides a statistical summary of the real-time Hg vapour data and simultaneously measured meteorological parameters (air temperature, relative humidity, relative pressure corrected to sea level, and wind speed). Appendix 1 of Rukhlov et al. (2020) provides time vs. Hg^0 in air and vs. meteorological parameters, wind direction, and Hg^0 in air statistical plots for each survey.

Measured Hg vapor concentrations of this study range from 0.5 to 54 $\text{ng}\cdot\text{m}^{-3}$, averaging $1.93 \pm 2.98 \text{ ng}\cdot\text{m}^{-3}$ ($n=9660$; Table 1). The median value of $1.40 \text{ ng}\cdot\text{m}^{-3}$ is consistent with the background Hg concentration in air of the northern hemisphere ($1.5 \text{ ng}\cdot\text{m}^{-3}$; Sprovieri et al., 2016).

5.1. British Columbia Geological Survey laboratory

To test the instrument, we measured air in the basement laboratory of the British Columbia Geological Survey at 1810 Blanshard Street in downtown Victoria in the presence of a benchtop laboratory mercury barometer (an undisturbed source of elemental Hg). We also took measurements in adjacent areas inside and outside of the building (Fig. 3). Our first test (July 25, 2020) revealed Hg vapour concentration up to 33 $\text{ng}\cdot\text{m}^{-3}$ near a W.M. Welch Scientific Company mercury barometer (Chicago, U.S.A.). Outside of the laboratory, 25 m away from the barometer, concentration was at the background level of $1.4 \text{ ng}\cdot\text{m}^{-3}$. In other areas of the laboratory, which are connected to a central heating, ventilating, and air-conditioning system, intermediate Hg vapour concentrations were observed. Measurements at the end of this study (August 28, 2020) reproduced these results (Table 1; Fig. 3). Up to 36 $\text{ng}\cdot\text{m}^{-3}$ of gaseous Hg^0 was measured in the air about 2 m above the floor,

Table 1. Statistical summary of real-time Hg vapour concentrations in near-surface air and simultaneously measured meteorological parameters.

Parameter	N	Mean	σ	Minimum	Percentiles					Maximum
					25	50	75	87	97	
All data of this study (24.07.2020-28.08.2020)										
Hg ⁰ in air (ng·m ⁻³)	9660	1.93	2.98	0.50	1.22	1.40	1.64	2.05	4.13	54.35
Air temperature (°C)	9289	19.2	3.6	12.1	15.5	19.5	22.4	23.2	24.8	30.9
Relative humidity (%)	9289	58.9	10.6	31.0	51.8	58.2	64.8	72.5	80.7	85.5
Relative pressure (hPa)	9289	1017.8	3.2	1007.2	1015.0	1018.3	1019.8	1021.0	1023.9	1025.1
Wind speed (m·s ⁻¹)	8915	0.8	0.8	0.0	0.0	0.6	1.2	1.7	2.7	6.3
British Columbia Geological Survey laboratory (25.07.2020, 15:20-15:26)										
Hg ⁰ in air (ng·m ⁻³)	35	19.90	8.94	1.34	19.10	20.71	25.95	30.20	32.90	33.05
Air temperature (°C)	35	23.2	0.4	22.4	23.0	23.4	23.4	23.5	23.5	23.5
Relative humidity (%)	35	48.2	0.8	47.5	47.6	47.8	48.6	49.5	50.1	50.1
Relative pressure (hPa)	35	1022.5	0.1	1022.4	1022.4	1022.5	1022.5	1022.5	1022.6	1022.6
Wind speed (m·s ⁻¹)	na	na	na	na	na	na	na	na	na	na
British Columbia Geological Survey laboratory (28.08.2020, 17:17-17:40)										
Hg ⁰ in air (ng·m ⁻³)	122	8.90	8.67	1.28	2.11	4.12	13.54	18.81	33.87	36.20
Air temperature (°C)	na	na	na	na	na	na	na	na	na	na
Relative humidity (%)	na	na	na	na	na	na	na	na	na	na
Relative pressure (hPa)	na	na	na	na	na	na	na	na	na	na
Wind speed (m·s ⁻¹)	na	na	na	na	na	na	na	na	na	na
Bear Hill (28.08.2020, 13:22-14:55)										
Hg ⁰ in air (ng·m ⁻³)	490	1.24	0.17	0.72	1.12	1.24	1.37	1.45	1.58	1.81
Air temperature (°C)	490	22.7	1.5	19.8	21.6	22.3	23.7	24.4	26.1	27.9
Relative humidity (%)	490	52.9	3.7	42.8	50.1	53.3	56.1	57.0	57.9	58.5
Relative pressure (hPa)	490	1018.1	0.5	1017.0	1017.9	1018.1	1018.5	1018.7	1019.0	1019.1
Wind speed (m·s ⁻¹)	490	0.7	0.6	0.0	0.0	0.6	0.9	1.3	2.0	3.8
Colwood (05.08.2020, 15:04-16:32)										
Hg ⁰ in air (ng·m ⁻³)	211	1.59	0.69	0.51	1.11	1.49	2.07	2.40	3.15	3.81
Air temperature (°C)	45	25.6	0.6	24.2	25.2	25.6	26.1	26.4	26.7	26.8
Relative humidity (%)	45	43.2	2.8	39.1	40.8	42.6	44.8	45.9	52.1	53.6
Relative pressure (hPa)	45	1012.6	2.5	1007.2	1010.7	1012.7	1014.5	1016.3	1016.8	1016.8
Wind speed (m·s ⁻¹)	45	0.9	1.0	0.0	0.0	0.8	1.3	1.7	3.5	3.5
Coronation Mountain (06.08.2020, 10:38-14:06)										
Hg ⁰ in air (ng·m ⁻³)	1099	1.79	0.69	0.57	1.47	1.64	1.88	2.29	3.05	10.85
Air temperature (°C)	1099	15.3	1.3	13.0	14.4	15.1	15.9	16.6	18.5	21.6
Relative humidity (%)	1099	64.5	4.6	51.0	62.0	64.4	67.0	69.5	73.6	79.1
Relative pressure (hPa)	1099	1013.0	0.9	1010.3	1012.3	1012.6	1013.5	1014.3	1015.0	1015.4
Wind speed (m·s ⁻¹)	1099	0.7	1.0	0.0	0.0	0.0	1.1	1.8	3.6	6.3
Coronation Mountain (12.08.2020, 10:19-15:49)										
Hg ⁰ in air (ng·m ⁻³)	1562	1.49	0.49	0.50	1.27	1.40	1.58	1.69	2.65	5.91
Air temperature (°C)	1562	14.8	1.1	12.4	13.9	14.9	15.6	16.1	16.9	18.2
Relative humidity (%)	1562	59.1	3.2	48.7	57.2	59.4	61.0	62.2	64.6	71.0
Relative pressure (hPa)	1562	1018.4	0.6	1016.8	1018.0	1018.4	1018.9	1019.1	1019.5	1019.8
Wind speed (m·s ⁻¹)	1562	1.1	0.9	0.0	0.4	0.9	1.7	2.2	3.1	5.2
Deep Cove (27.08.2020, 13:24-15:02)										
Hg ⁰ in air (ng·m ⁻³)	519	1.27	0.19	0.78	1.16	1.27	1.38	1.46	1.60	3.06
Air temperature (°C)	519	22.6	0.9	20.3	22.1	22.7	23.2	23.6	24.2	25.0
Relative humidity (%)	519	53.0	3.2	46.4	51.0	52.5	54.4	56.5	61.1	63.6
Relative pressure (hPa)	519	1018.6	0.3	1017.8	1018.4	1018.7	1018.9	1019.0	1019.3	1019.4
Wind speed (m·s ⁻¹)	519	0.7	0.8	0.0	0.0	0.5	1.1	1.6	2.7	4.3

Table 1. Continued.

Parameter	N	Mean	σ	Minimum	Percentiles					Maximum
					25	50	75	87	97	
Durance Lake (19.08.2020, 16:02-16:58)										
Hg ⁰ in air (ng·m ⁻³)	298	1.18	0.21	0.75	1.04	1.17	1.30	1.38	1.58	2.55
Air temperature (°C)	298	22.9	0.5	21.8	22.6	22.9	23.1	23.2	24.1	24.5
Relative humidity (%)	298	56.6	2.4	50.5	55.1	56.2	58.3	59.4	61.8	63.0
Relative pressure (hPa)	298	1013.4	0.4	1012.5	1013.1	1013.5	1013.6	1013.8	1014.1	1014.2
Wind speed (m·s ⁻¹)	298	0.6	0.6	0.0	0.0	0.5	1.0	1.3	1.7	2.2
Elk Lake (28.08.2020, 15:39-16:07)										
Hg ⁰ in air (ng·m ⁻³)	152	1.22	0.17	0.55	1.13	1.22	1.33	1.41	1.55	1.67
Air temperature (°C)	152	20.2	0.4	19.7	20.0	20.1	20.4	20.6	21.4	21.6
Relative humidity (%)	152	63.1	2.6	56.9	61.9	63.2	65.2	65.8	67.1	67.9
Relative pressure (hPa)	152	1017.9	0.2	1017.4	1017.7	1017.9	1018.1	1018.1	1018.2	1018.3
Wind speed (m·s ⁻¹)	152	0.8	0.7	0.0	0.0	0.7	1.3	1.8	2.2	2.5
Goldstream (22.08.2020, 11:50-13:23)										
Hg ⁰ in air (ng·m ⁻³)	494	4.21	8.62	0.59	1.26	1.41	1.67	3.71	34.18	54.35
Air temperature (°C)	494	19.5	0.6	18.1	19.1	19.6	19.9	20.1	20.7	21.1
Relative humidity (%)	494	59.9	5.5	49.4	55.8	58.8	63.6	67.0	71.4	73.7
Relative pressure (hPa)	494	1022.5	0.6	1020.8	1022.0	1022.3	1022.9	1023.2	1023.9	1024.2
Wind speed (m·s ⁻¹)	494	0.4	0.5	0.0	0.0	0.0	0.8	1.1	1.4	2.3
Harling Point (08.08.2020, 15:23-16:19)										
Hg ⁰ in air (ng·m ⁻³)	239	1.59	0.20	1.08	1.46	1.57	1.69	1.78	2.10	2.45
Air temperature (°C)	238	16.1	1.3	12.9	15.3	15.9	16.7	17.4	19.3	21.5
Relative humidity (%)	238	73.0	4.8	56.1	71.1	74.1	75.8	77.3	81.0	85.5
Relative pressure (hPa)	238	1024.6	0.3	1024.0	1024.3	1024.8	1024.9	1024.9	1025.0	1025.1
Wind speed (m·s ⁻¹)	238	1.3	0.7	0.0	0.7	1.2	1.7	2.2	2.8	3.2
Jordan River (17.08.2020, 09:57-12:51)										
Hg ⁰ in air (ng·m ⁻³)	917	1.35	0.18	0.83	1.22	1.34	1.47	1.55	1.69	1.96
Air temperature (°C)	917	19.3	1.1	17.4	18.6	19.0	19.7	20.2	22.5	24.9
Relative humidity (%)	917	78.5	3.9	62.2	77.3	79.3	80.9	81.9	83.0	84.5
Relative pressure (hPa)	917	1020.3	1.1	1018.1	1019.6	1020.1	1020.5	1021.3	1024.0	1024.5
Wind speed (m·s ⁻¹)	917	0.4	0.5	0.0	0.0	0.0	0.6	0.9	1.6	3.7
Mount Washington (25.08.2020, 13:00-15:37)										
Hg ⁰ in air (ng·m ⁻³)	789	2.27	1.80	0.50	1.41	1.83	2.69	3.28	5.49	16.35
Air temperature (°C)	789	15.9	1.9	12.1	14.5	15.6	17.0	18.3	20.0	22.0
Relative humidity (%)	789	66.7	6.7	47.0	62.9	67.0	71.5	73.8	78.4	81.3
Relative pressure (hPa)	789	1015.5	1.1	1012.2	1014.7	1015.6	1016.3	1016.7	1017.2	1017.6
Wind speed (m·s ⁻¹)	625	1.2	0.7	0.3	0.6	1.0	1.6	2.1	2.8	3.9
Skirt Mountain (10.08.2020, 11:43-16:15)										
Hg ⁰ in air (ng·m ⁻³)	1325	2.15	2.97	0.51	1.23	1.44	1.71	2.37	15.44	19.23
Air temperature (°C)	1325	23.4	1.5	20.7	22.3	23.2	24.2	24.9	27.0	30.9
Relative humidity (%)	1325	53.2	4.5	38.4	50.2	52.9	56.9	58.6	60.9	65.6
Relative pressure (hPa)	1325	1020.0	0.8	1018.0	1019.4	1019.9	1020.7	1020.9	1021.3	1022.1
Wind speed (m·s ⁻¹)	1325	0.5	0.6	0.0	0.0	0.4	0.8	1.1	1.7	3.4
Sooke Hills (11.08.2020, 14:17-16:43)										
Hg ⁰ in air (ng·m ⁻³)	769	1.30	0.20	0.74	1.17	1.29	1.42	1.53	1.73	1.92
Air temperature (°C)	769	20.4	0.9	18.5	19.7	20.4	21.1	21.6	22.2	23.1
Relative humidity (%)	769	41.6	4.7	31.0	38.3	41.8	45.0	46.0	48.7	57.4
Relative pressure (hPa)	769	1014.1	0.7	1013.0	1013.7	1013.9	1014.4	1014.9	1015.9	1016.5
Wind speed (m·s ⁻¹)	769	1.0	0.8	0.0	0.4	0.8	1.4	1.9	2.7	5.2

Table 1. Continued.

Parameter	N	Mean	σ	Minimum	Percentiles					Maximum
					25	50	75	87	97	
Tod Inlet (27.08.2020, 16:15-17:28)										
Hg ⁰ in air (ng·m ⁻³)	382	1.17	0.17	0.58	1.06	1.17	1.27	1.35	1.49	2.06
Air temperature (°C)	382	23.1	0.5	21.6	22.8	23.0	23.3	23.6	24.3	25.1
Relative humidity (%)	382	47.3	2.0	43.8	46.0	46.9	48.2	49.1	52.7	53.6
Relative pressure (hPa)	382	1017.4	0.2	1017.0	1017.3	1017.4	1017.6	1017.7	1017.9	1018.2
Wind speed (m·s ⁻¹)	382	0.7	0.7	0.0	0.0	0.5	1.1	1.5	2.4	3.4
Victoria (25.07.2020, 14:56-15:20)										
Hg ⁰ in air (ng·m ⁻³)	130	1.76	0.32	1.18	1.51	1.76	1.96	2.19	2.39	2.51
Air temperature (°C)	130	22.8	0.6	21.2	22.4	22.9	23.2	23.4	23.8	24.2
Relative humidity (%)	130	48.8	1.1	46.8	48.0	48.8	49.5	50.1	51.3	51.6
Relative pressure (hPa)	130	1022.8	0.3	1022.4	1022.6	1022.7	1022.8	1023.1	1023.6	1023.8
Wind speed (m·s ⁻¹)	na	na	na	na	na	na	na	na	na	na

Real-time Hg vapour mass concentrations in near-surface air (in nanograms per cubic metre, ng·m⁻³) measured via a portable RA-915M Zeeman mercury atomic absorption spectrometer with high frequency modulated light polarization. Meteorological parameters simultaneously measured using a Kestrel 5500 meter. Relative pressure (in hectopascal, hPa) adjusted to sea-level (see text for details). N - number of values used to calculate the statistics; σ - standard deviation; na - not analyzed.

immediately near the barometer. Mercury vapour concentration gradually decreases with distance from the Hg⁰ source. Mercury vapour concentrations in ambient air of the adjacent areas outside the laboratory, including stairwell and breezeway enclosures, were above the background Hg (1.77-5.31 ng·m⁻³) and diluted to background further away from the laboratory on both basement levels and immediately outside the building (Fig. 3). These results show that an undisturbed, open source of Hg⁰ such as the laboratory mercury barometer generates a stable Hg vapour halo in the ambient air of a positively ventilated, closed area more than 25 m away from the source. Because our measurements identified an environmental exposure issue, the mercury barometer has been sealed in a plastic bag and removed to permanently ventilated chemical storage.

5.2. Coronation Mountain; Lara-Coronation polymetallic volcanogenic massive sulphide occurrence

The Lara-Coronation volcanogenic massive sulphide (VMS) Zn-Cu-Pb-Ag-Au occurrence is on southern flank of Coronation Mountain (Fig. 1; MINFILE 092B 129) and, with only one bedrock exposure, is mostly covered by up to 30 m of glacial sediments (Figs. 4, 5; Bodnar, 2017; Heberlein et al., 2017). We carried out surveys along a forest road, spur trails, and across a clearcut under slightly different conditions on two separate days. Air was sampled 10-50 cm above ground on August 6, 2020, following several days and nights of rain. The second survey, on August 12, 2020, sampled air 1-10 cm above ground after six days without precipitation. Air temperature was similar, but atmospheric pressure was higher and relative humidity slightly lower on August 12th compared to those on August 6th. Predominantly west-southwest wind calmed by mid-day on August 6th, whereas predominantly east-southeast wind was generally consistent on August 12th (Table 1;

Appendix 1 in Rukhlov et al., 2020).

The Lara-Coronation polymetallic occurrence comprises two lenses (up to 16 m thick) of banded and massive sphalerite, pyrite, chalcopyrite, and galena with minor tetrahedrite, tennantite, bornite, electrum, pearceite, and arsenopyrite (Northcote and Muller, 1972; Kelso and Wetherup, 2008; Wetherup, 2010; Ruks, 2015; Bodnar, 2017). The mineralization is hosted by greenschist-facies, sheared and silicified felsic and intermediate volcanic rocks of the McLaughlin Ridge Formation (Sicker Group; Middle to Late Devonian), which dip steeply northeast. Samples of massive sulphide ore yielded up to 90 ppm Hg (Kelso and Wetherup, 2008; Bodnar, 2017) that is four orders of magnitude higher than the Clarke value for the Earth's crust (45 ppb Hg; Rudnick and Gao, 2005). Associated mineralization includes chalcopyrite-pyrite stringers in silicified shear zones and pyrite-rich horizons (Figs. 5, 6).

Previous multi-media geochemical studies at Lara reported up to 460 ppb Hg in soils and up to 133 ppb Hg in vegetation (Bodnar, 2017; Heberlein et al., 2017 and references therein). However, the Hg dispersion haloes in these media are not entirely linked to the polymetallic mineralization, because anomalous Hg concentrations cluster mainly above a barren pyrite-rich horizon a few hundred metres upslope, to the northeast (Fig. 7). In contrast, anomalous Hg vapour haloes were detected in near-surface air directly above the sediment-covered Lara-Coronation VMS mineralized zones, regardless of the overburden thickness, air sampling height, soil moisture, and meteorological conditions (Figs. 8, 9). Concentrations of gaseous Hg⁰ in air range from 0.57 to 11 ng·m⁻³ with the median (background) value of 1.64 ng·m⁻³ on August 6th (n=1099) and from 0.50 to 5.9 ng·m⁻³ with the median (background) value of 1.40 ng·m⁻³ on August 12th (n=1562; Table 1). The strongest anomalies (4 to 7x background Hg) occur above the high-grade

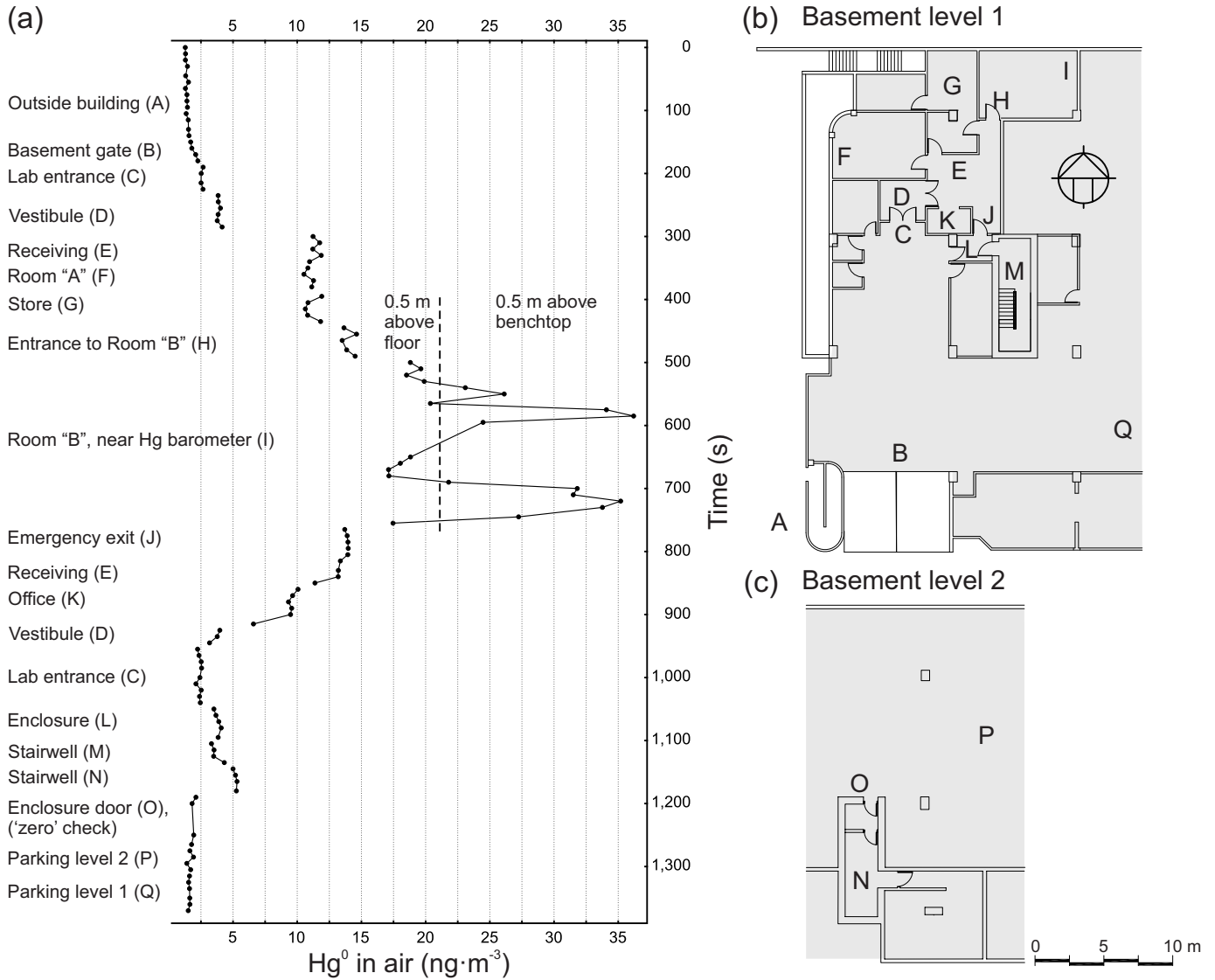


Fig. 3. Real-time Hg vapour concentrations in ambient air of the British Columbia Geological Survey laboratory and adjacent areas on August 28, 2020. **a)** Hg^0 in air ($ng \cdot m^{-3}$) vs. time (in seconds) plot. **b)** Sampling locations on basement level 1 and outside the buildings. **c)** Sampling locations on basement level 2.



Fig. 4. Glacigenic overburden above the Lara-Coronation polymetallic volcanogenic massive sulphide occurrence.



Fig. 5. Outcrop of volcanogenic massive sulphide mineralization in sheared felsic volcanic rocks of the McLaughlin Ridge Formation (Sicker Group; Late to Middle Devonian) at the Lara-Coronation occurrence.



Fig. 6. Closeup of chalcopyrite-pyrite stringers in a silicified shear zone at the Lara-Coronation occurrence.

ore in a flooded trench and on a nearby outcrop of mineralized volcanic rocks (Figs. 8, 9). Weaker Hg vapour haloes in near-surface air also mark polymetallic VMS zone buried under 30 m of glacial sediments, silicified shear zones with sulphide stringers, pyrite-rich horizon, and a northwest-trending thrust fault (Fig. 9). In addition, conspicuous Hg vapour emissions were measured above Nanaimo Group sedimentary rocks in the footwall of a northwest-trending thrust fault on August 6, 2020, but not on August 12, 2020 (Figs. 8, 9).

5.3. Mount Washington; Mount Washington Copper porphyry Cu-Mo-Au and Domineer-Lakeview epithermal Au-Ag-Cu mineralization

On the northern ridge of Mount Washington (Fig. 1), the Mount Washington Copper past producer (MINFILE 092F 117) and Domineer-Lakeview developed prospect (MINFILE 092F 116) represent porphyry Cu-Mo-Au to high-sulphidation epithermal Au-Ag-Cu mineralization (Carson, 1960a, b, 1968;

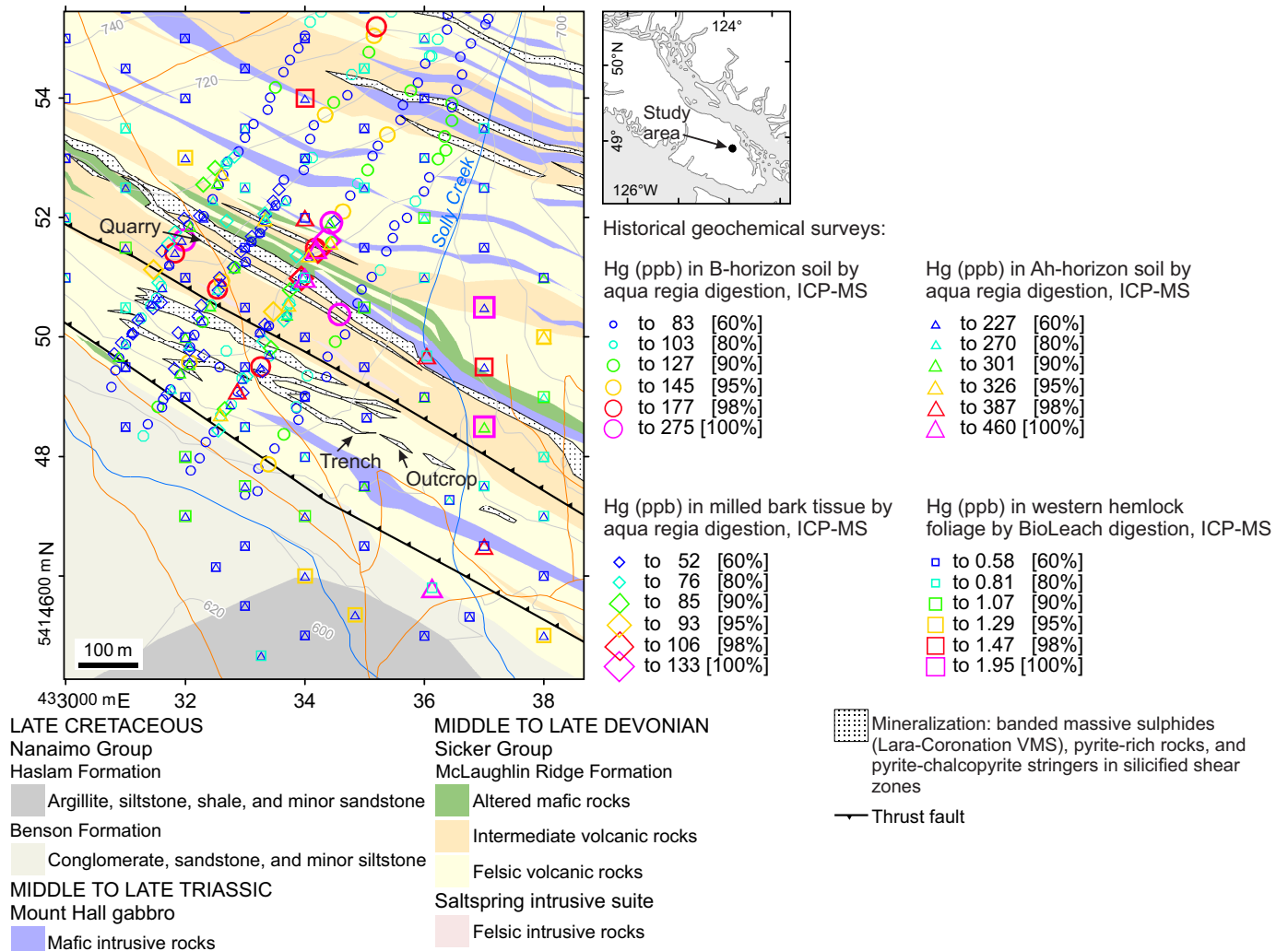


Fig. 7. Percentile-ranked Hg concentrations in soil and vegetation at the Lara-Coronation occurrence. Compiled geochemical data from Bodnar (2017) and Heberlein et al. (2017). Geology after Muller (1977), Massey et al. (1991, 1994), Massey (1995), Wetherup (2010), Ruks (2015), and Bodnar (2017).

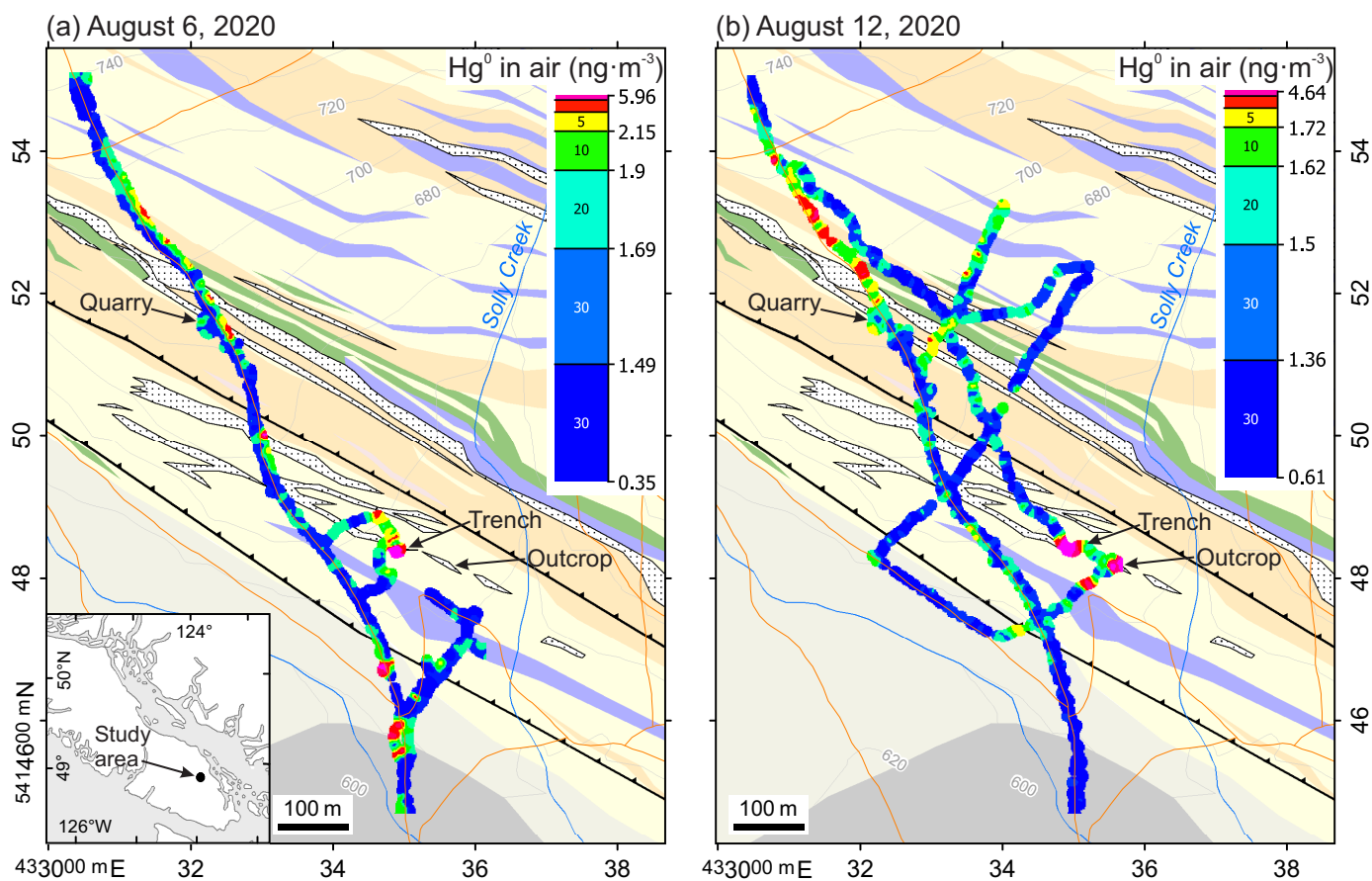


Fig. 8. Percentile-gridded, real-time Hg vapour concentrations ($\text{ng}\cdot\text{m}^{-3}$) in near-surface air at the Lara-Coronation occurrence. Gridding interpolation based on modified inverse distance weighing method. Geology legend as in Figure 7. **a)** Hg vapour concentrations in air 10-50 cm above ground on August 6, 2020. **b)** Hg vapour concentrations in air 1-10 cm above ground sampled using a hose on August 12, 2020.

Neville, 1963; Stevenson, 1967; Northcote and Muller, 1972; McDougall, 1987; Muller, 1989; Houle, 2019). We surveyed across an open pit at Mount Washington Copper and along a trail to a trench at the Domineer zone, less than 400 m to the south (Figs. 10, 11).

The area is underlain by mafic volcanic rocks of the Karmutsen Formation (Vancouver Group; Late Triassic) that are unconformably overlain by siliciclastic rocks of the Comox Formation (Nanaimo Group; Late Cretaceous). The youngest rocks are intermediate and felsic porphyry stocks, dikes, sills, and late breccias of the Mount Washington plutonic suite and related volcanoclastic strata (Eocene to Oligocene). Detachment faults along bedding of the sedimentary and volcanoclastic rocks are offset by variably trending, high-angle faults (Muller, 1989; Houle, 2019). The late breccias host the polymetallic sulphide mineralization, which was discovered in 1940.

Both Mount Washington Copper and Domineer-Lakeview are flat-lying bodies (1-7.6 m thick). At Mount Washington Copper, a chalcopyrite-pyrite-quartz vein stockwork and disseminated sulphides continue for more than 750 m along the contact between the Comox Formation and an overlying diorite sill of the Mount Washington plutonic suite (Fig. 12). The Domineer-Lakeview zone comprises quartz-pyrite-arsenopyrite breccia

with banded sulphides, veins, and lenses within pervasive kaolinite and chlorite (outer envelope) alteration for 1.5 km along a detachment fault. Ore minerals identified at both occurrences include chalcopyrite, tetrahedrite-tennantite, arsenopyrite, realgar (Fig. 13), orpiment, bornite, covellite, chalcocite, molybdenite, arsenic, chalcostibite, sphalerite, galena, and hessite (Neville, 1963; Houle, 2019).

Mercury vapour concentrations in air 10-50 cm above ground range from 0.50 to 16 $\text{ng}\cdot\text{m}^{-3}$, with a median (background) value of 1.83 $\text{ng}\cdot\text{m}^{-3}$ ($n=789$; Table 1). Prominent Hg^0 haloes in near-surface atmosphere (up to 9x background Hg) mark exposed massive arsenopyrite-pyrite±chalcopyrite±realgar veins at both the Mount Washington Copper southern open pit and Domineer trench (Figs. 10, 11). Slightly elevated Hg vapour haloes (1.3-1.5x background Hg) also occur above breccia about 100 m south of the open pit. These subtle anomalies were not detected in initial measurements taken one hour earlier, although duplicated data show consistent Hg vapour concentrations elsewhere, regardless of fluctuating meteorological conditions (Fig. 11; Appendix 1 of Rukhlov et al., 2020). We attribute the discrepancy to the combined effects of wind gusts, which were up to 4 $\text{m}\cdot\text{s}^{-1}$, increased atmospheric pressure, and decreased air temperature, which may have diluted and suppressed emission

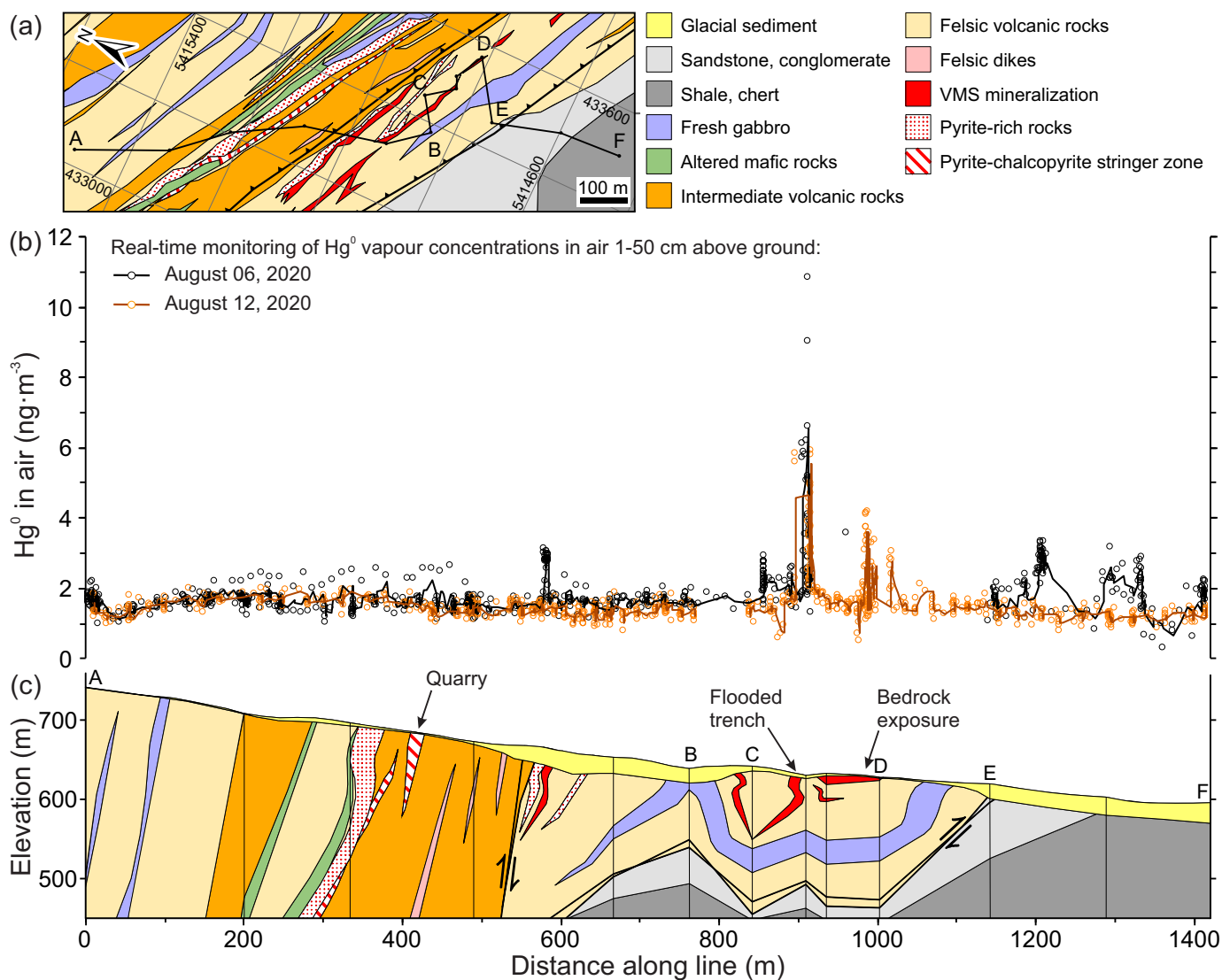


Fig. 9. a) Bedrock geology of the Lara-Coronation occurrence and position of section lines for b) and c); modified after Massey et al. (1991, 1994), Massey (1995), Wetherup (2010), and Bodnar (2017). b) Profile showing Hg⁰ (ng·m⁻³) in near-surface air on August 6, 2020 (sampling height 10-50 cm above ground; black symbols) and August 12, 2020 (sampling height 1-10 cm above ground; beige symbols) and corresponding average curves. c) Northwest-southeast cross section; overburden thickness after Bodnar (2017).

of gaseous Hg⁰ from the surface into the atmosphere during the initial measurements.

5.4. Jordan River; Sunro Cu-Ag-Au sulphide occurrence

The Sunro occurrence is on the eastern side of the Jordan River canyon (Figs. 1, 14) and is a past-producing underground deposit (Fig. 15; MINFILE 092C 073). The deposit is hosted by basalts of the Metchosin Formation that are intruded by a steeply dipping, wide (several 100 m), medium- to coarse-grained, hornblende gabbro dike whose trend is parallel to a northwesterly fold axis in the volcanic rocks (Clapp, 1912; Brewer, 1918; Erich and Blanshard, 1921; Guelpa and Meusy, 1971; Meusy, 1971; Muller, 1977; Massey et al., 1994). Outliers of marine sandstones and conglomerates of the Sooke Formation (Carmanah Group; Eocene to Oligocene)

unconformably overlie the basalts and gabbro both to the southwest and northeast. Sulphide Cu-Ag-Au mineralization is localized in subvertical hornblendized shear zones (up to 40 m wide) in basalts adjacent to the dike. Ore minerals include mainly chalcopyrite, bornite, pyrite, and pyrrhotite, with minor native copper, molybdenite, arsenopyrite, cubanite and pentlandite. They form gash veinlets, lenticular masses, smears, and blebs (Starr and Frith, 1926; Toombs, 1951).

Mercury vapour concentrations in air 1-10 cm above ground along the traverse across the intrusive contact, several mineralized zones, and faults show a normal distribution (Appendix 1 in Rukhlov et al., 2020) and range from 0.83 to 2.0 ng·m⁻³, averaging 1.35 ng·m⁻³ (n=917; Table 1). Overburden is seemingly thin (<2 m?), with bedrock exposed in steep banks and quarries along a trail to the River portal (Fig. 15). The

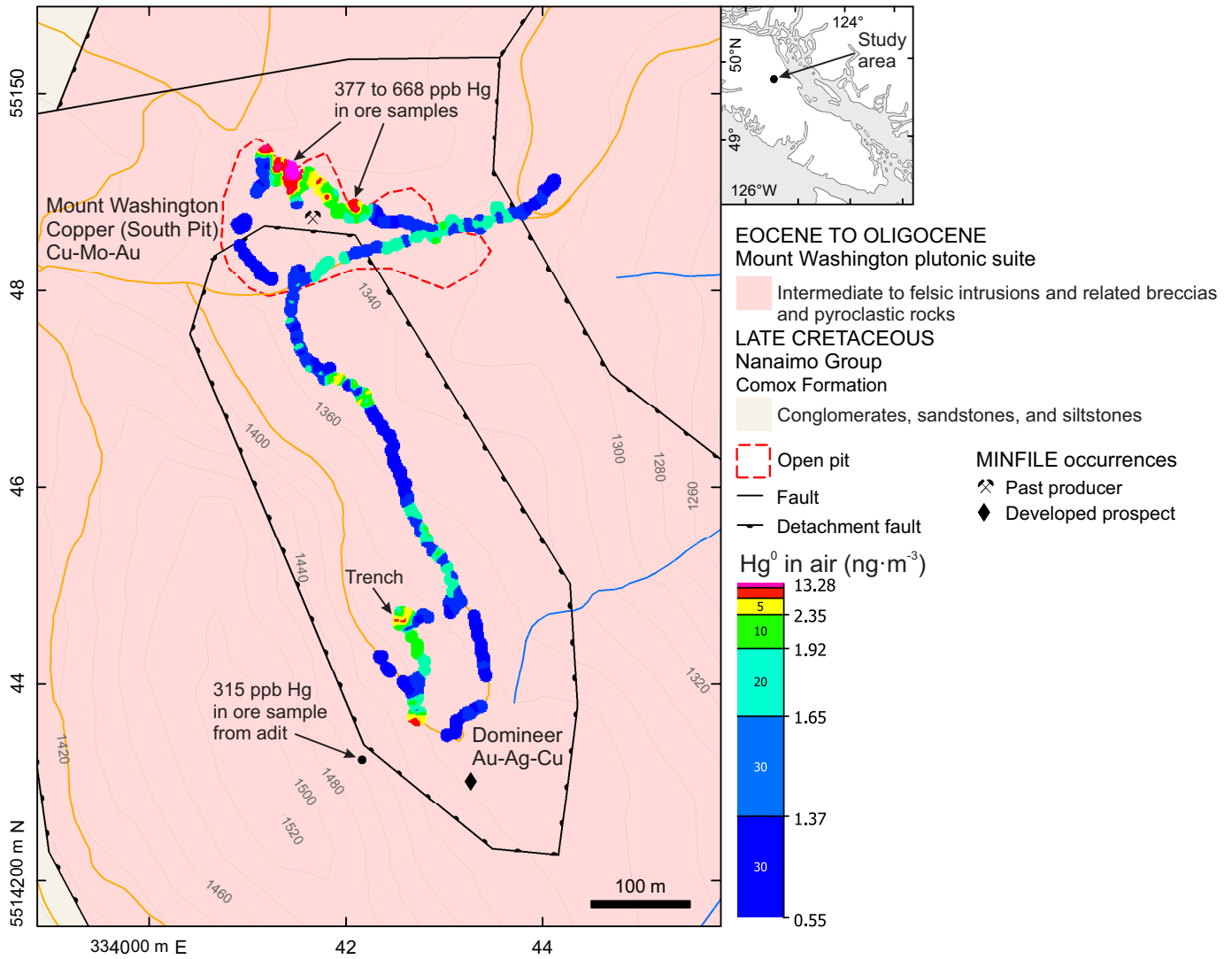


Fig. 10. Percentile-gridded, real-time Hg vapour concentrations ($\text{ng}\cdot\text{m}^{-3}$) in air 10-50 cm above ground at Mount Washington Copper and Domineer mineralization. Gridding interpolation based on modified inverse distance weighing method. Geology after Cui et al. (2017, 2018) based on Carson (1960a, b, 1968), Stevenson (1967), Northcote and Muller (1972), Muller (1977, 1989), McDougall (1987), and Massey et al. (1994). Concentrations of Hg in ore samples from Houle (2000; 2019).

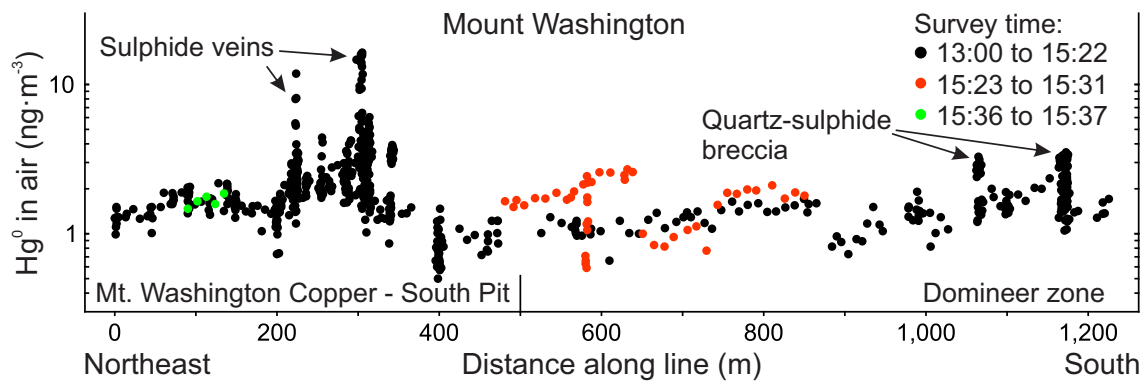


Fig. 11. Profile for Hg⁰ in air ($\text{ng}\cdot\text{m}^{-3}$) with respect to distance along traverse (m) for Mount Washington Copper and Domineer occurrences (see Figure 10).



Fig. 12. Flat-lying quartz-sulphide mineralized zone beneath diorite sill, Mount Washington Copper.



Fig. 13. Realgar in quartz-sulphide mineralized zone at Mount Washington Copper.

strongest Hg^0 haloes (top 5 percentile: $1.7\text{--}2.0 \text{ ng}\cdot\text{m}^{-3}$) are at what appears to be intersection of the mineralized northwest-striking River fault and west-northwest Central fault, and above the intrusive contact offset by a north-south fault immediately south of the B.C. Electric Forebay reservoir (Fig. 14). Several weaker Hg vapor haloes (95th percentile: $1.6\text{--}1.7 \text{ ng}\cdot\text{m}^{-3}$) also mark the Cave and Central zones and faults. Meteorological conditions were generally stable, and a spike in barometric pressure in the middle of the survey had little impact on the background Hg^0 in air (Appendix 1 in Rukhlov et al., 2020).

5.5. Goldstream Park area; vein gold occurrence (Bentley); Cu-Ag-Au sulphide occurrence at Skirt Mountain (Ralph)

We conducted two surveys north of the town of Goldstream (Figs. 1, 16). One was along a trail through Goldstream Park that extends to the quartz vein Bentley Au occurrence (MINFILE 092B 067), the other along the flank of Skirt Mountain that

includes the sulphide Cu-Ag-Au Ralph occurrence (MINFILE 092B 014). Since the discovery of placer gold in the Goldstream River in 1858, the area has attracted much prospecting, with intermittent underground exploration and mining taking place until the late 1930s (Neumann, 1991; Yorath, 2005).

The Bentley Au occurrence is hosted by pervasively sheared ribbon chert, argillite, slate, phyllite, schist, and metavolcanic rocks of the Leech River complex (Jurassic to Cretaceous). An adit was driven along a quartz vein in schistose rocks and a shaft sunk upslope, about 40 m to the west (Fig. 16). The Ralph Cu-Ag-Au occurrence is hosted by interbedded silicified dacite tuff and cherty argillite of the Leech River complex that are cut by steeply dipping shear zones in the footwall of an east-dipping thrust fault that juxtaposes gneisses of the Wark-Colquitz complex (Wrangell terrane, Paleozoic to Jurassic) above the Leech River rocks (Fig. 16). The mineralization comprises en echelon lenses (0.15–1.2 m wide) of massive chalcopyrite, pyrrhotite, pyrite, and chalcocite with quartz and calcite. For brief periods between 1897 and 1938, an underground mine produced 6655 kg Cu, 11.94 kg Ag, and 63 g Au (Neumann, 1991). Quaternary sediments of the Colwood delta cover bedrock in the southwestern corner of the area (Fig. 16).

Mercury vapour concentrations in air 10–50 cm above ground along the Goldstream Park traverse range from 0.59 to $54 \text{ ng}\cdot\text{m}^{-3}$, with a median (background) value of $1.41 \text{ ng}\cdot\text{m}^{-3}$ ($n=494$; Table 1). The maximum Hg vapour concentration ($54 \text{ ng}\cdot\text{m}^{-3}$) is above a small pit on overgrown tailings from a nearby shaft (Figs. 16, 17a). However, air directly above the shaft shows background Hg, and only up to 3x background Hg in air at the entrance to the adit 40 m to the east (down slope). Such a strong Hg emission from the tailings suggests that Hg amalgamation might have been used to recover gold from crushed ore at the Bentley mine. Mercury amalgamation was extensively used by the mining industry between the mid-1800s and early 1900s (e.g., Higuera et al., 2012; Dalziel and Tordon, 2014). A few weak Hg anomalies ($1.7\text{--}3.6 \text{ ng}\cdot\text{m}^{-3}$) also occur on a ridge immediately south of Bentley occurrence.

Concentrations of Hg^0 in air 1–10 cm above ground on the western flank of Mount Skirt range from 0.51 to $19 \text{ ng}\cdot\text{m}^{-3}$ with the median (background) value of $1.44 \text{ ng}\cdot\text{m}^{-3}$ ($n=1325$; Table 1). The maximum value marks an adit at the Ralph occurrence (Fig. 17b). Anomalous Hg^0 haloes (up to $5.4 \text{ ng}\cdot\text{m}^{-3}$) extend from the nearby oxidized tailings for more than 100 m to the southeast. Another conspicuous Hg vapour anomaly (up to $3.9 \text{ ng}\cdot\text{m}^{-3}$) is 280 m to the northeast, above gneisses of the Wark-Colquitz complex in the hanging wall of the terrane-bounding thrust fault. Elevated Hg vapour haloes ($1.9\text{--}2.4 \text{ ng}\cdot\text{m}^{-3}$) also highlight the thrust fault (Figs. 16, 17b). Changing weather conditions during both surveys have little effect on the anomalous Hg vapour haloes in near-surface atmosphere (Appendix 1 in Rukhlov et al., 2020).

5.6. Sooke Hills and Colwood; Leech River fault and related splays

The Sooke Hills survey, south of the town of Goldstream

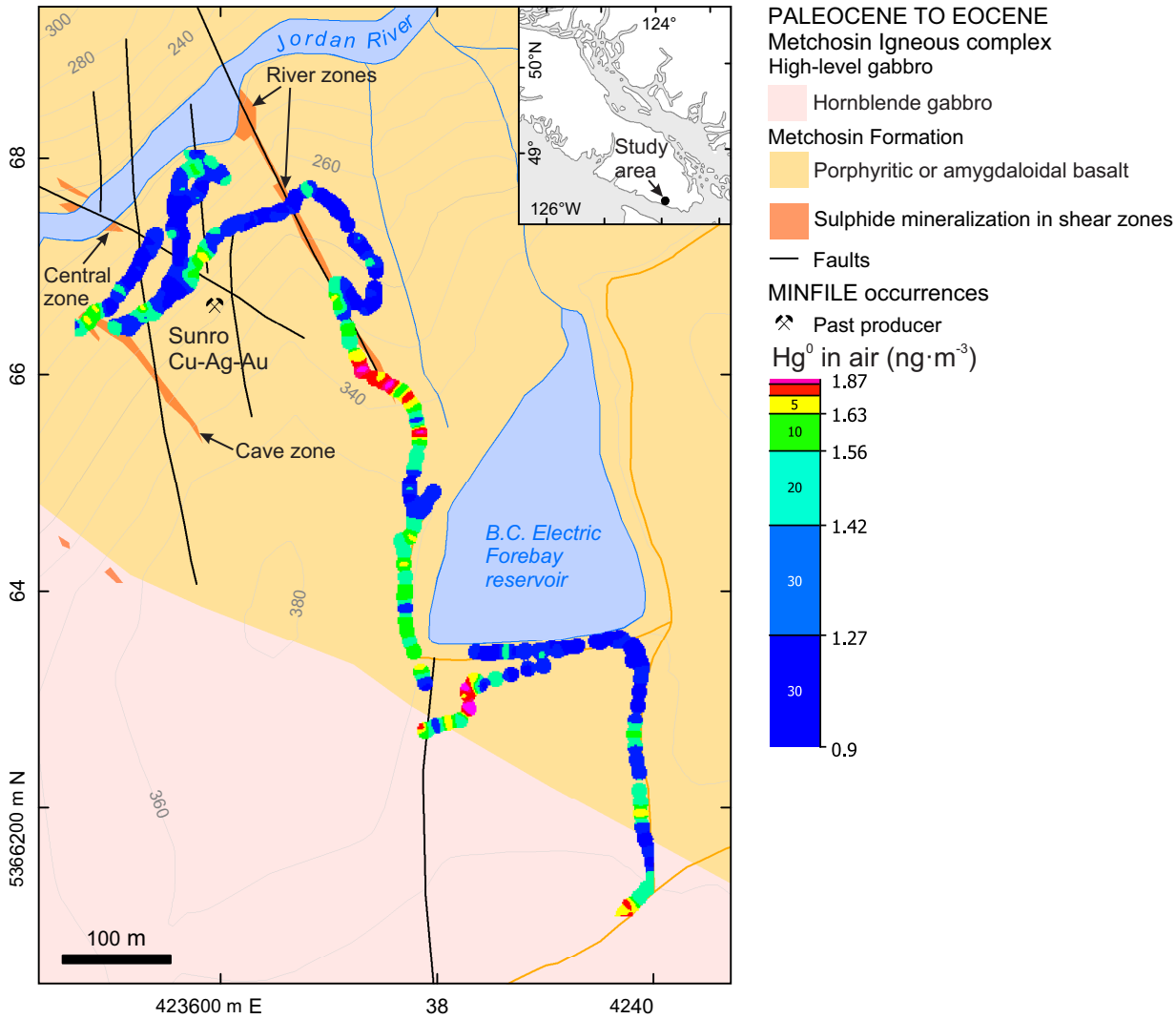


Fig. 14. Percentile-gridded, real-time Hg vapour concentrations ($\text{ng}\cdot\text{m}^{-3}$) in air 1-10 cm above ground at the Sunro occurrence. Gridding interpolation based on modified inverse distance weighing method. Geology after Cui et al. (2017, 2018) based on Clapp (1912), Brewer (1918), Erich and Blanshard (1921), Guelpa and Meusy (1971), Meusy (1971), Muller (1977), and Massey et al. (1994).



Fig. 15. Sealed adit through the main ore zone (River) at the Sunro occurrence.

(Fig. 1), used the Sooke Hills Wilderness trail to traverse across the Leech River thrust fault, which juxtaposes cherty argillite, slate, phyllite, and schist interbedded with minor metavolcanic rocks of the Pacific Rim terrane (Leech River complex; Jurassic to Cretaceous) to the north against massive and pillowed basalt, basaltic hyaloclastite breccia, tuff, and rare limestone of the Metchosin Formation (Crescent terrane, Metchosin Igneous complex; Paleocene to Eocene) to the south (Fig. 18). A splay approximately 0.6 km to the southwest cuts volcanic rocks of the Metchosin Formation. Bedrock is locally exposed along the trail close to the thrusts. Metchosin Formation rocks display open folds, with fold axis trending parallel to the strike of the thrust faults. In the hanging wall, pervasively sheared Leech River complex rocks display a subvertical foliation concordant with the thrust (Clapp, 1912, 1913; Muller, 1977, 1980, 1983; Massey et al., 1994; Yorath, 2005).

Mercury vapour concentrations in air 1-10 cm above ground

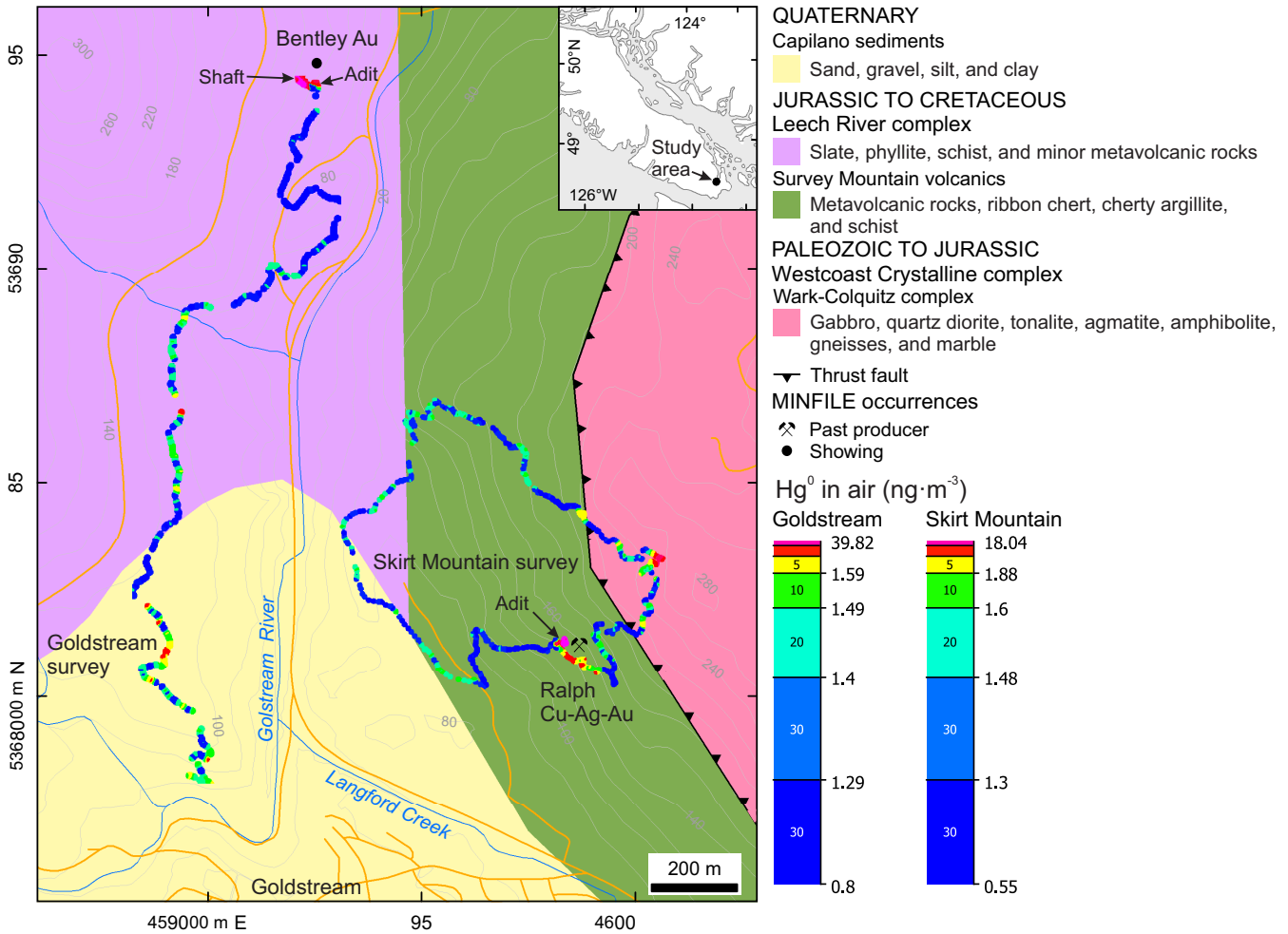


Fig. 16. Percentile-gridded, real-time Hg vapour concentrations (ng·m⁻³) in near-surface air along a trail to the Bentley Au vein occurrence in Goldstream park (sampling height 10-50 cm above ground) and on the western flank of Skirt Mountain, across the Ralph sulphide Cu-Ag-Au occurrence (sampling height 1-10 cm). Gridding interpolation is based on modified inverse distance weighing method. Geology after Cui et al. (2017, 2018) based on Clapp (1912, 1913), Muller (1977, 1980, 1983), and Massey et al. (1994).

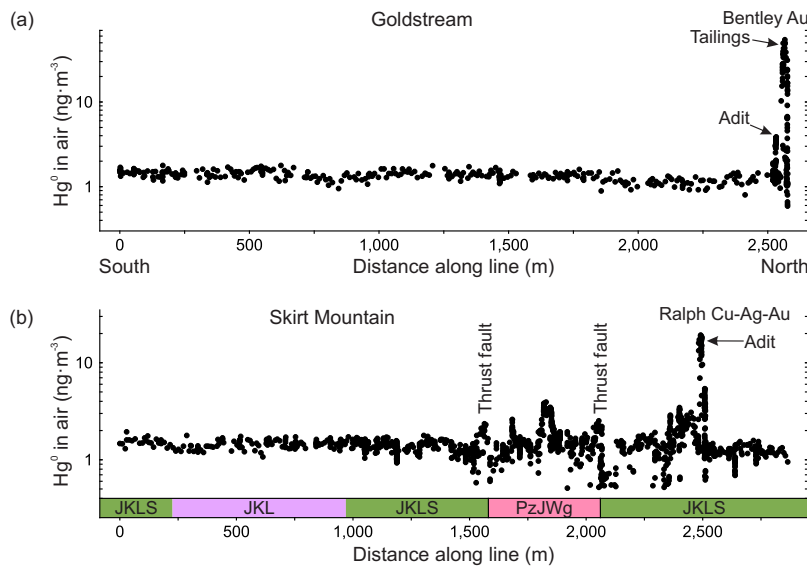


Fig. 17. Profiles for Hg⁰ in air (ng·m⁻³) with respect to distance along traverse (m) for Goldstream Park area (see Figure 16). **a)** Goldstream Park, Bentley occurrence. **b)** Skirt Mountain; Ralph occurrence, and Wrangell terrane-Pacific Rim terrane boundary; the traverse was in a loop hence the units are repeated.

show a normal distribution (Appendix 1 in Rukhlov et al., 2020) and range from 0.74 to 1.9 ng·m⁻³, averaging 1.30 ng·m⁻³ (n=769; Table 1). The top 5 percentile values (1.6-1.9 ng·m⁻³) highlight both the Leech River fault, which has a history of Quaternary movement (Morell et al., 2017), and its splay (Figs. 18, 19). Two anomalous Hg⁰ haloes also occur between the Leech River fault and its splay, possibly marking additional buried splays. A positive spike in atmospheric pressure accompanied by an increased wind speed slightly suppressed the background Hg vapour concentration during the survey but did not mask the elevated Hg⁰ emission above the Leech River fault (Appendix 1 of Rukhlov et al., 2020).

We also took measurements at Colwood, about 6 km southeast of the Sooke Hills, along roads and trails through Royal Roads University campus. Here, the along-strike continuation of the Leech River fault dips steeply northeast, juxtaposing intrusive and metamorphic rocks of the Westcoast Crystalline complex (Paleozoic to Jurassic) above basalts of the Metchosin Formation to the southwest. A subparallel splay of the Leech River fault cuts basalts of the Metchosin Formation about 0.5 km to the southwest. Sand and gravel (up to 60 m thick) of the Colwood delta (Capilano sediments; Quaternary) cover bedrock. Mercury concentrations range from 0.51 to 3.8 ng·m⁻³, averaging 1.59 ng·m⁻³ (n=211; Table 1; Appendix 1 of Rukhlov et al., 2020). Values greater than 2.7 ng·m⁻³ (90th percentile) were measured above Westcoast Crystalline complex rocks. Slightly elevated concentrations (1.7-2.3 ng·m⁻³) coincide with the extrapolated splay fault to the southwest.

5.7. Durance Lake; northwest-striking fault between Wark-Colquitz complex and Bonanza Group (Wrangell terrane)

This survey traversed across a northwest-striking, high-angle fault that places Wark-Colquitz gneisses (Paleozoic to Jurassic) against Late Triassic to Middle Jurassic volcanic and sedimentary rocks of the Bonanza Group (Fig. 20). Wark-Colquitz gneisses are exposed south of the Durance Lake and volcanic rocks of the Bonanza Group outcrop along the northern shore of the lake (Fig. 20). Concentrations of Hg⁰ in air 10-50 cm above ground range from 0.75 to 2.6 ng·m⁻³, averaging 1.18 ng·m⁻³ (n=298; Table 1). The anomalous Hg values greater than 1.75 ng·m⁻³ highlight the fault (Fig. 21), regardless of the minor variations in atmospheric conditions (Appendix 1 in Rukhlov et al., 2020).

5.8. Elk Lake; northwest-striking fault between Wark-Colquitz complex and Karmutsen Formation (Wrangell terrane)

About 5 km southeast of the Durance Lake survey, we traversed across the continuation of the same high-angle northwest-striking fault, but where it juxtaposes Wark-Colquitz gneisses with mafic volcanic rocks of the Karmutsen Formation (Vancouver Group; Figs. 1, 22). The survey was conducted along the western shore of Elk Lake to evaluate Hg vapour emission above the bedrock units and the fault buried under a fringe (<2 m thick?) of Quaternary sediments. Mercury vapour

concentrations in air 10-50 cm above ground show a normal distribution (Appendix 1 in Rukhlov et al., 2020), ranging from 0.55 to 1.7 ng·m⁻³ with an average value of 1.22 ng·m⁻³ (n=152; Table 1). Some of the top 5 percentile values (>1.5 ng·m⁻³) occur above the buried fault, but three other spikes occur within 150 m on both sides of the fault, perhaps marking splays (Figs. 22, 23).

5.9. Tod Inlet; northeast-striking strike-slip fault

This survey extends from the north shore of Tod Inlet on the western side of central Saanich Peninsula east to Quarry Lake, the site of an historical limestone quarry (Figs. 1, 24). We traversed across a northeast striking strike-slip fault that cuts mafic volcanic rocks of the Karmutsen Formation (Vancouver Group; Middle to Late Triassic), limestones of the Quatsino Formation (Vancouver Group; Middle to Late Triassic), and unconformably overlying mafic to felsic volcanic and sedimentary rocks of the Bonanza Group (Late Triassic to Middle Jurassic). Overburden thickness is less than 5 m, with bedrock locally exposed along the profile.

Mercury vapour concentrations in air 10-50 cm above ground range from 0.58 to 2.1 ng·m⁻³, averaging 1.17 ng·m⁻³ (n=382; Table 1). The strongest Hg vapour halo (up to 2.1 ng·m⁻³) marks the sediment-covered strike-slip fault, and several weaker haloes (>95th percentile: 1.4-1.6 ng·m⁻³) occur above the volcanic and sedimentary rocks of the Bonanza Group and along the contact with limestone of the Quatsino Formation (Figs. 24, 25). Meteorological conditions were relatively consistent during the survey (Appendix 1 of Rukhlov et al., 2020).

5.10. Deep Cove; northwest-striking thrust faults

Granitic rocks of the Saanich batholith (Island plutonic suite; Early to Middle Jurassic) and unconformably overlying siliciclastic rocks of the Nanaimo Group (Late Cretaceous) are offset by several northwest-striking thrust faults at Deep Cove on the western side of northern Saanich Peninsula (Figs. 1, 26). Air was sampled 1-10 cm above ground across the sediment-covered unconformity and one of the thrust faults and its splay, which place the granitoids exposed at Warrior Point against gently north-dipping Nanaimo Group sandstones exposed along the shore to the northwest. Concentrations of Hg⁰ in air range from 0.78 to 3.1 ng·m⁻³, averaging 1.27 ng·m⁻³ (n=519; Table 1). The top 5 percentile values (>1.53 ng·m⁻³) occur above granitic rocks immediately north of the thrust fault, with some 90th percentile values marking sandstones near the unconformity (Figs. 26, 27). Minor fluctuations in atmospheric conditions did not have a notable effect on Hg⁰ in air (Appendix 1 in Rukhlov et al., 2020).

5.11. Bear Hill; intrusive contact between Island plutonic suite and Karmutsen Formation mafic volcanic rocks

This survey traversed along a road and a trail to the summit of Bear Hill in central Saanich Peninsula, extending across quartz diorite and granodiorite at the southwestern margin of

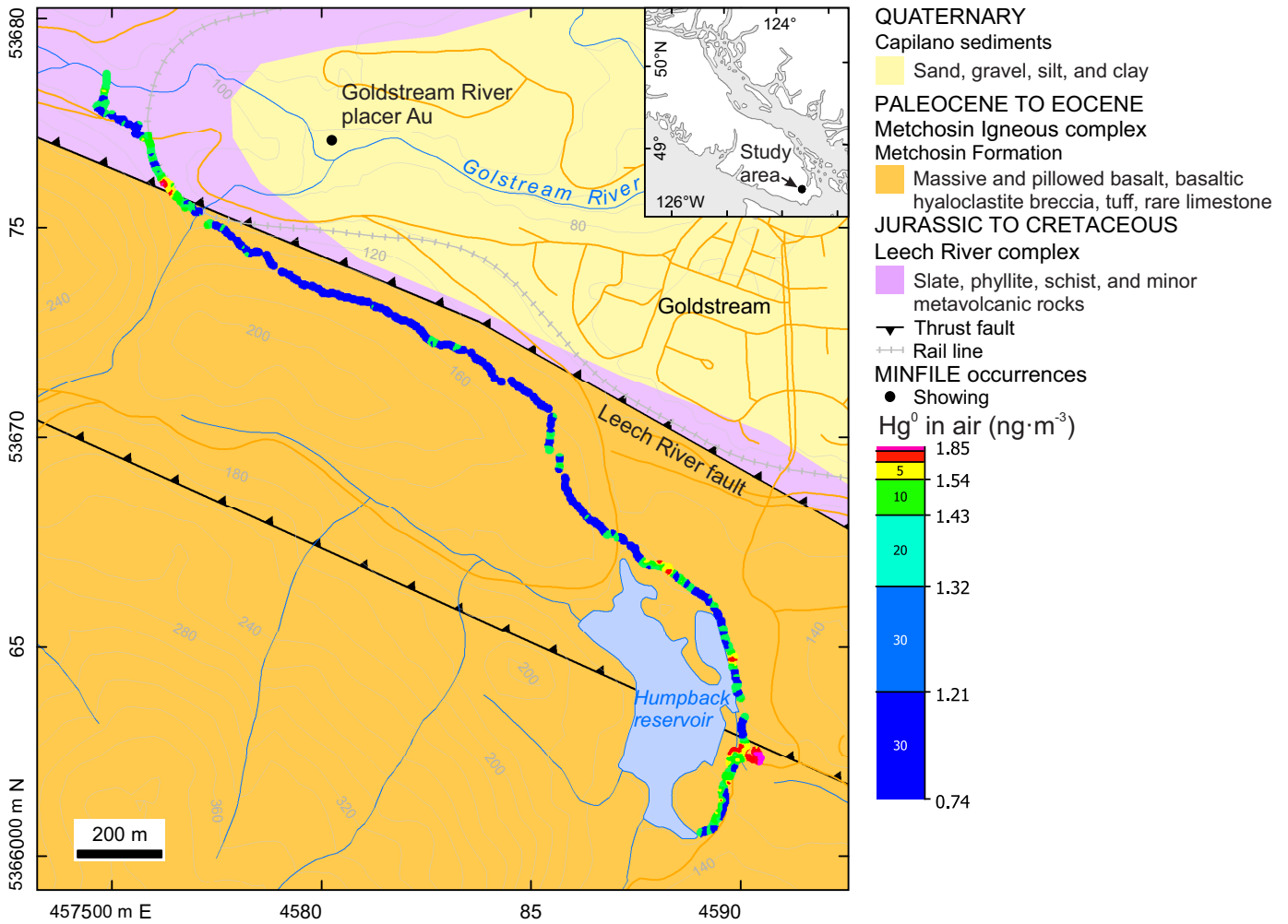


Fig. 18. Percentile-gridded, real-time Hg vapour concentrations (ng·m⁻³) in air 1-10 cm above ground at Sooke Hills. Gridding interpolation based on modified inverse distance weighing method. Geology after Cui et al. (2017, 2018) based on Clapp (1912, 1913), Muller (1977, 1980, 1983), and Massey et al. (1994).

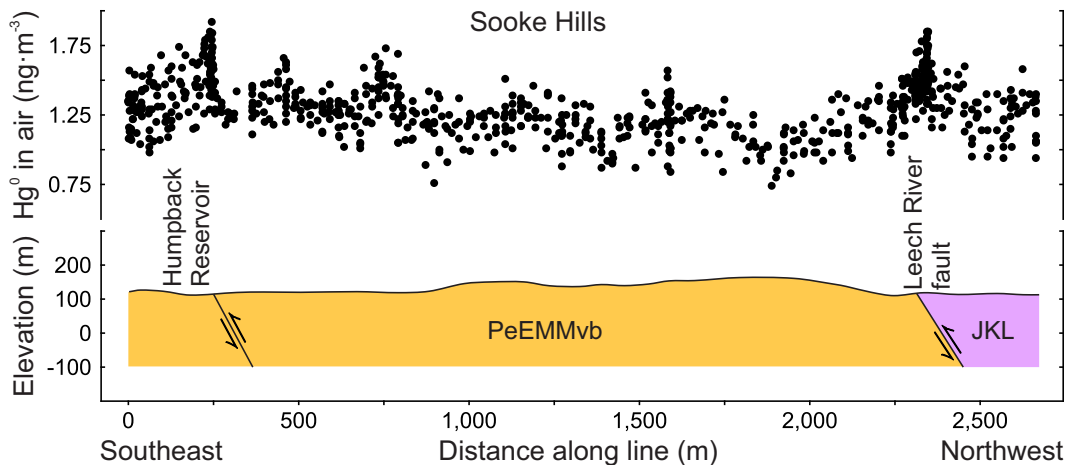


Fig. 19. Profile for Hg⁰ in air (ng·m⁻³) with respect to distance along traverse (m) and geological cross-section at Sooke Hills (see Figure 18).

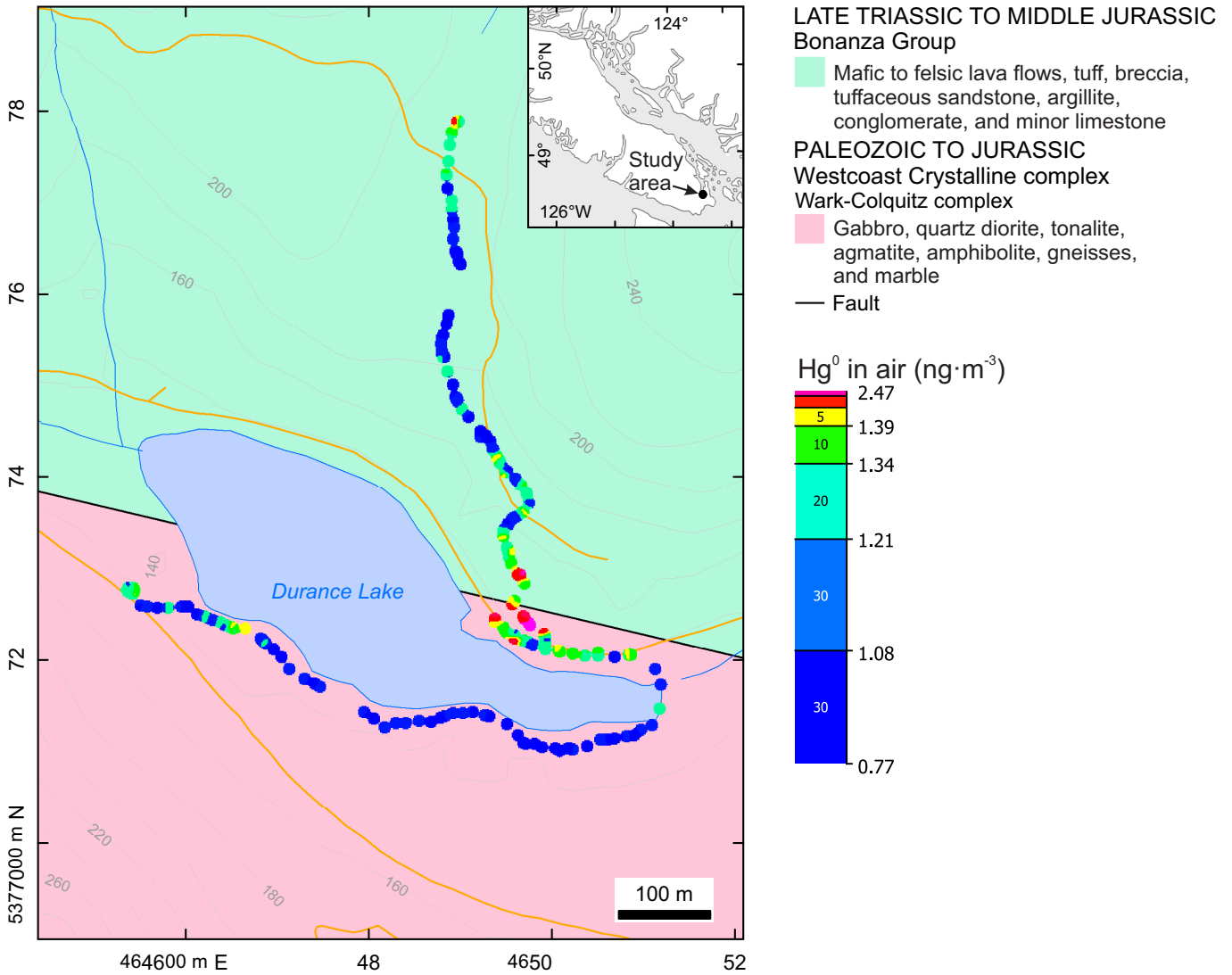


Fig. 20. Percentile-gridded, real-time Hg⁰ vapour concentrations (ng·m⁻³) in air 10-50 cm above ground at Durance Lake, west-central Saanich Peninsula. Gridding interpolation based on modified inverse distance weighing method. Geology modified after Cui et al. (2017, 2018) based on Clapp (1912, 1913), Muller (1977, 1980, 1983), and Massey et al. (1994).

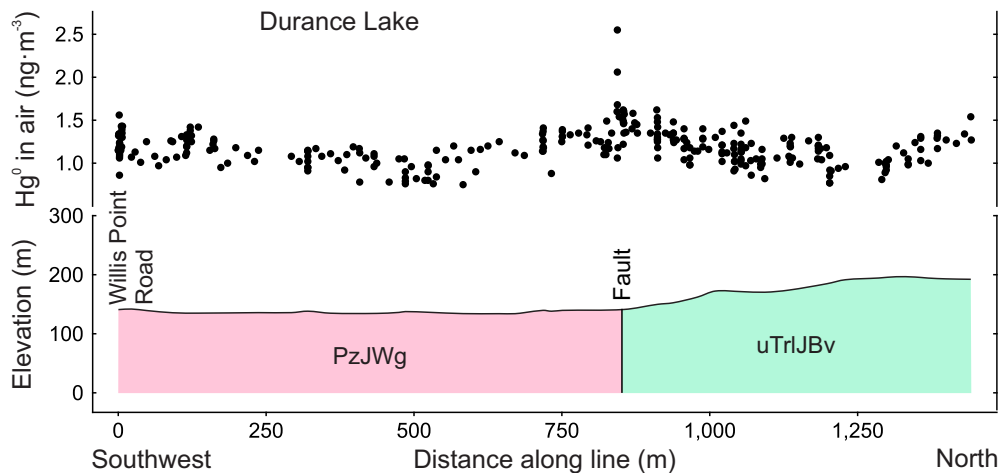


Fig. 21. Profile for Hg⁰ in air (ng·m⁻³) with respect to distance along traverse (m) and geological cross-section at Durance Lake (see Figure 20).

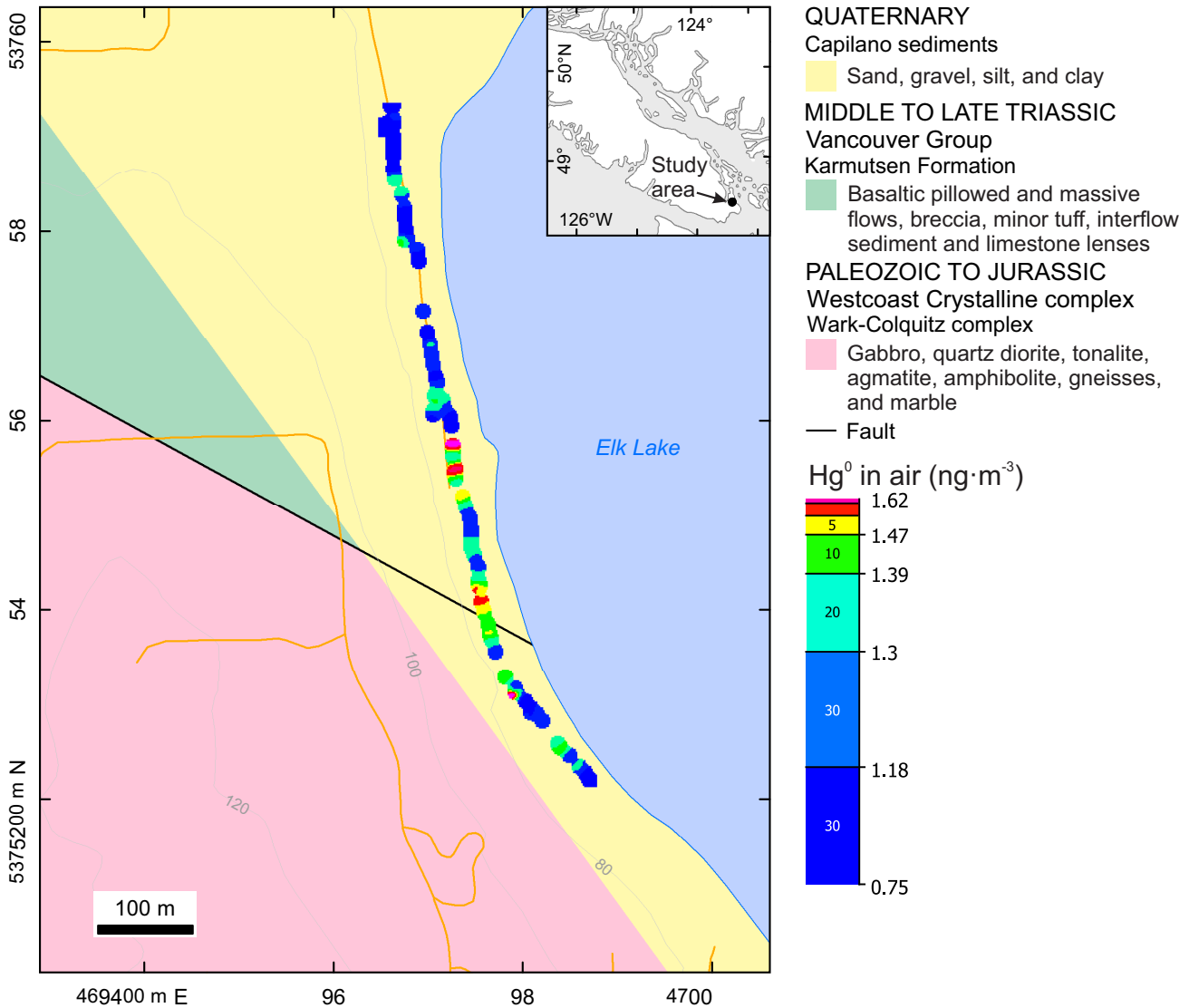


Fig. 22. Percentile-gridded, real-time Hg vapour concentrations (ng·m⁻³) in air 10-50 cm above ground at Elk Lake, central Saanich Peninsula. Gridding interpolation based on modified inverse distance weighing method. Geology after Cui et al. (2017, 2018) based on Clapp (1912, 1913), Muller (1977, 1980, 1983), and Massey et al. (1994).

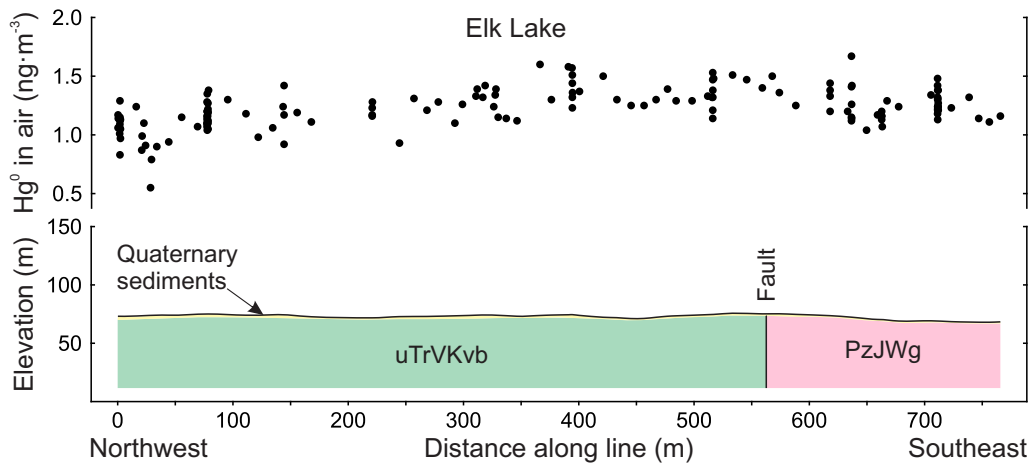


Fig. 23. Profile for Hg⁰ in air (ng·m⁻³) with respect to distance along traverse (m) and geological cross-section at Elk Lake (see Figure 22).

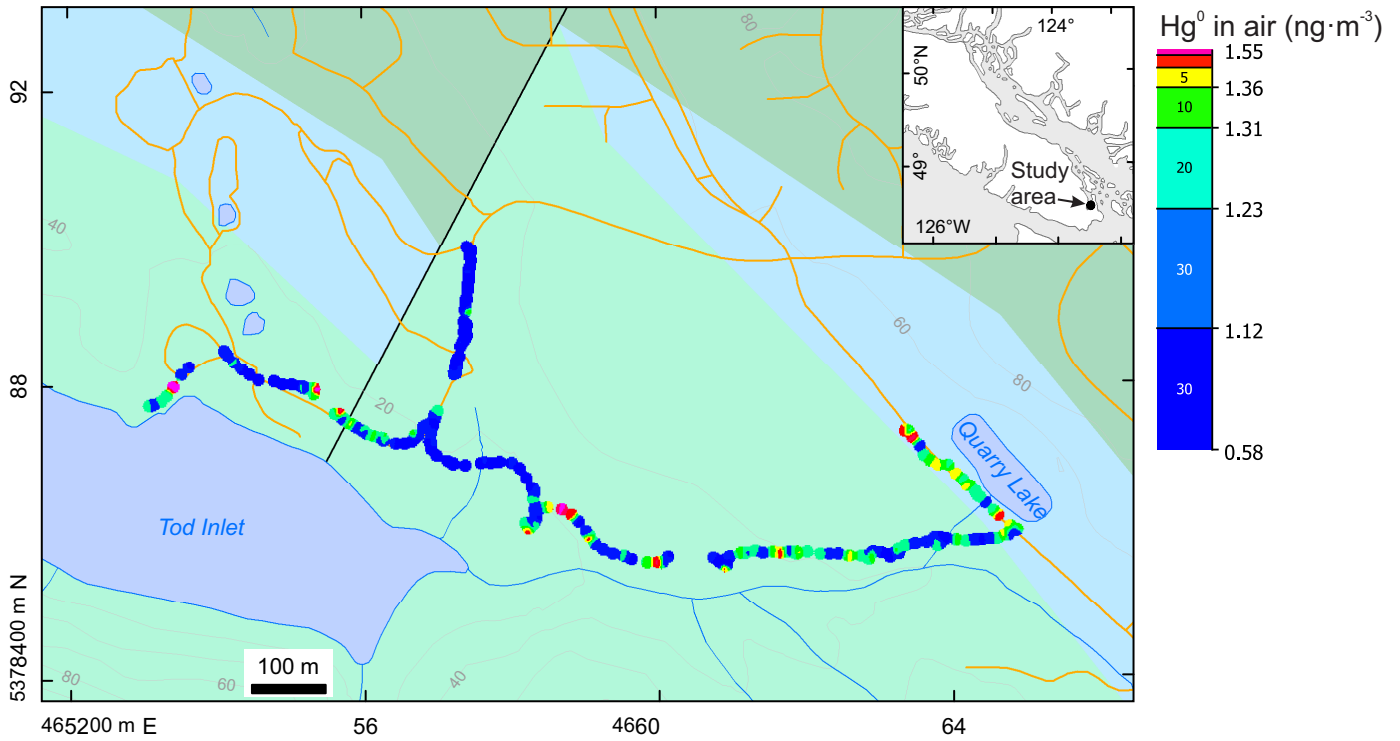


Fig. 24. Percentile-gridded, real-time Hg vapour concentrations (ng·m⁻³) in air 10-50 cm above ground at Tod Inlet, west-central Saanich Peninsula. Gridding interpolation based on modified inverse distance weighing method. Geology after Cui et al. (2017, 2018) based on Clapp (1912, 1913), Muller (1977, 1980, 1983), and Massey et al. (1994).

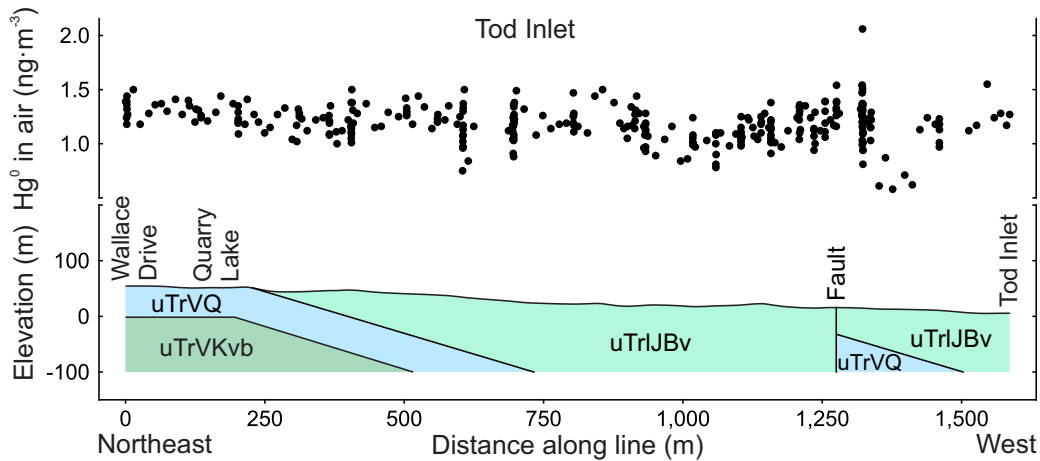


Fig. 25. Profile for Hg⁰ in air (ng·m⁻³) with respect to distance along traverse (m) and geological cross-section at Tod Inlet (see Figure 24).

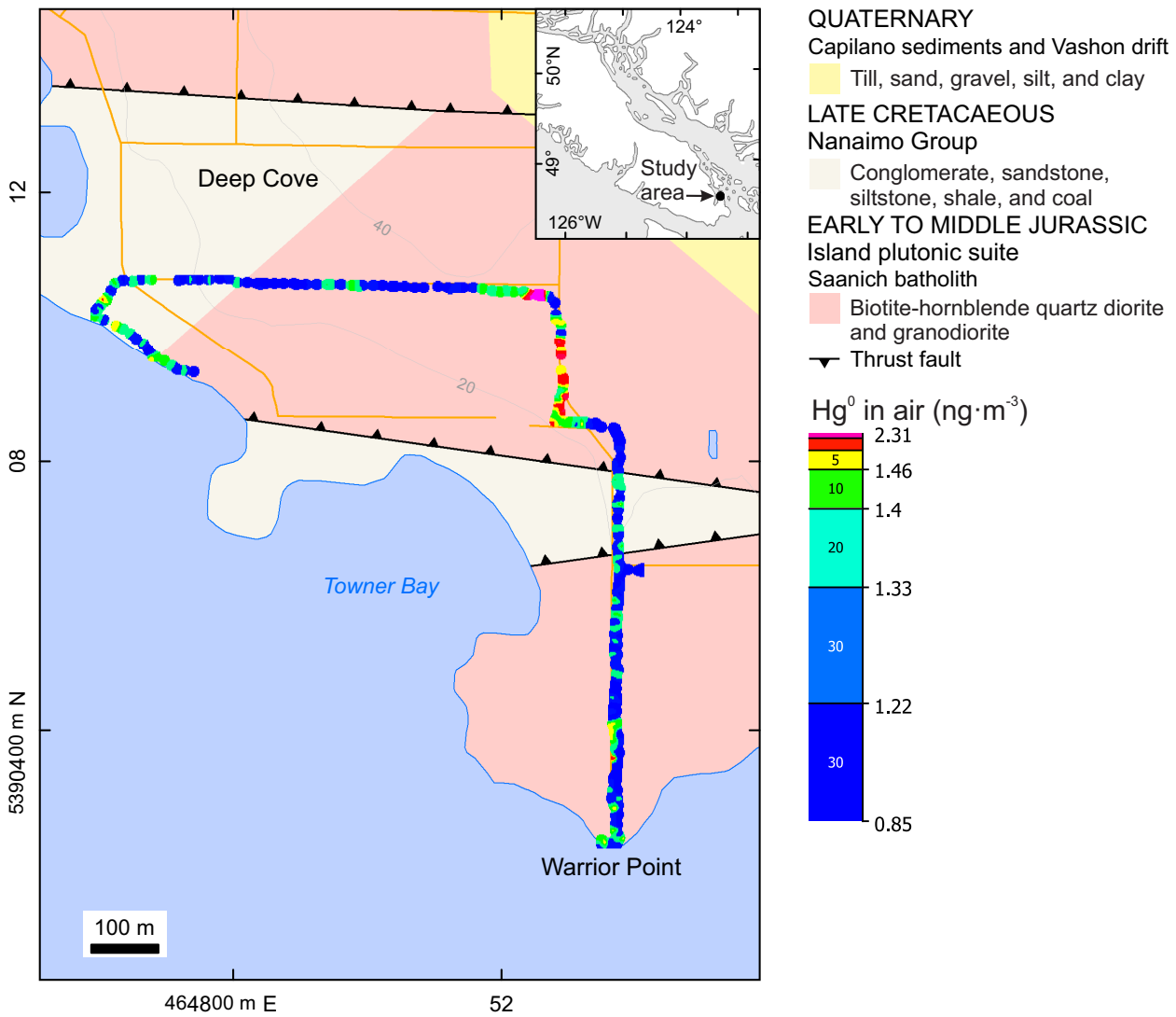


Fig. 26. Percentile-gridded, real-time Hg vapour concentrations (ng·m⁻³) in air 1-10 cm above ground at Deep Cove, northern Saanich Peninsula. Gridding interpolation based on modified inverse distance weighing method. Geology after Cui et al. (2017, 2018) based on Clapp (1912, 1913), Muller (1977, 1980, 1983), and Massey et al. (1994).

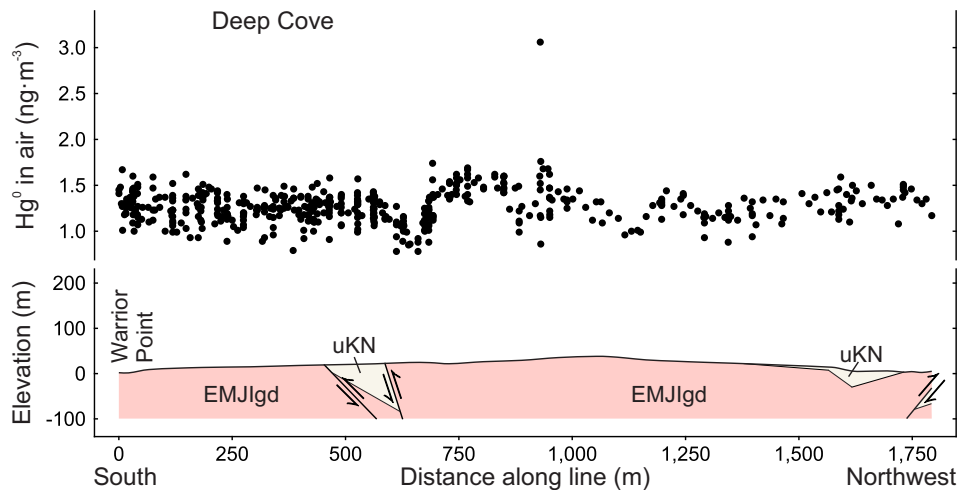


Fig. 27. Profile for Hg⁰ in air (ng·m⁻³) with respect to distance along traverse (m) and geological cross-section at Deep Cove (see Figure 26).

the Saanich batholith (Island plutonic suite; Early to Middle Jurassic) that cut mafic volcanic rocks of the Karmutsen Formation (Figs. 1, 28). Although bedrock is well exposed, no volcanic rocks were observed along the trail, suggesting that the intrusive contact is farther west than portrayed on currently available maps (Figs. 28, 29). Mercury vapour concentrations show normal distribution, ranging from 0.72 to 1.8 ng·m⁻³, averaging 1.24 ng·m⁻³ (n=490; Table 1; Appendix 1 of Rukhlov et al., 2020). The top 5 percentile spikes are spread for about 200 m above the granitoids exposed along the trail. Because volcanic rocks are not exposed along the survey profile, the elevated Hg emanations may mark the Saanich batholith margin. Data collected along the same traverse twice within 1.5 hrs were similar (Fig. 29), regardless of subtle changes in meteorological conditions. Changing weather might have influenced the Hg vapour concentrations. As wind speed and relative pressure decreased and air temperature increased, concentrations of Hg⁰ in air also increased (Appendix 1 of Rukhlov et al., 2020). Therefore, the scattered elevated Hg haloes at Bear Lake might simply reflect changing meteorological conditions.

5.12. Central Victoria: Harling Point and downtown

At Harling Point, in the municipality of Oak Bay east of downtown Victoria, possible tectonic mélangé deposits including radiolarian chert, greywacke, mafic volcanic rocks, argillite, pebbly mudstones, and limestone clast-bearing breccias of the Pandora Peak unit (Pacific Rim terrane) are in thrust contact with Wark-Colquitz gneisses (Wrangell terrane; Rusmore and Cowan, 1985). We sampled air 1-10 cm above ground across strongly deformed rocks that are exposed in a northwest-striking shear zone. Mercury vapour concentrations in near-surface atmosphere range from 1.1 to 2.5 ng·m⁻³, averaging 1.59 ng·m⁻³ (n=239; Table 1; Appendix 1 of Rukhlov et al., 2020). The terrain-bounding fault is marked by the anomalous Hg vapor haloes in excess of 1.98 ng·m⁻³ (top 5 percentile).

To test Hg vapour levels in the urban air, we took measurements in downtown Victoria, which is underlain by intrusive and metamorphic rocks of the Westcoast Crystalline complex (Wark-Colquitz gneiss; Paleozoic to Jurassic) that are offset by northwest-striking faults and a series of northeast-striking cross-faults. Hornblende-plagioclase and quartz-feldspar gneisses and amphibolites display northwest-striking, moderately to steeply dipping foliation (Clapp, 1912, 1913; Muller, 1977, 1980, 1983; Massey et al., 1994; Yorath, 2005). Mercury vapour concentrations range from 1.2 to 2.5 ng·m⁻³, averaging 1.76 ng·m⁻³ (n=130; Table 1). The area underlain by quartz-feldspar Colquitz gneiss along Mount Stephen Avenue and Haultain Street has generally higher gaseous Hg⁰ emission (>95th percentile: 2.3-2.5 ng·m⁻³) compared to that underlain by amphibolite, agmatite, metadiorite, metagabbro, and hornblende-plagioclase Wark gneiss to the southwest (<2.2 ng·m⁻³), except for one of the three consecutive values (1.4, 1.7, and 2.4 ng·m⁻³) at the same location. A positive spike in relative pressure during the survey had little effect on the

measured Hg vapour concentration in near-surface air; wind speed and direction were not monitored during the survey (Appendix 1 of Rukhlov et al., 2020).

6. Discussion

By surveying 15 sites on southern Vancouver Island, including those with different types of mineralization (Table 2), this study evaluates the effectiveness of real-time Hg vapour sampling of near-surface atmosphere (i.e., layer of air 1-50 cm above ground) as a simple and instant technique for mineral exploration and geologic mapping in overburden-covered areas.

6.1. Mercury vapour haloes above mineralization

Our results show that the strongest anomalies mark auriferous quartz (Bentley Au occurrence; 38.5x background Hg) and Cu-Ag-Au sulphide veins (Ralph occurrence; 13.4x background Hg) at the Goldstream and Skirt Mountain localities (Figs. 16, 17). The highest Hg vapour concentrations in air (up to 54 ng·m⁻³) above a fresh pit hole in tailings at the Bentley Au occurrence indicate that amalgamation was likely used on site to recover gold. Exposed epithermal Au-Ag-Cu sulphide veins at Mount Washington (8.9x background Hg; Figs. 10, 11) and sediment-covered polymetallic VMS mineralization at the Lara-Coronation occurrence (4.2 to 6.6x background Hg; Figs. 8, 9) also have strong Hg vapour haloes. Ore samples from these occurrences contain up to 90 ppm Hg, which is four orders of magnitude higher than the average crustal abundance (45 ppb Hg; Rudnick and Gao, 2005), possibly concentrated in sphalerite and tennantite-tetrahedrite (Kelso and Wetherup, 2008; Bodnar, 2017). The Hg vapour anomalies in near-surface air above the polymetallic VMS zone buried under 30 m of glacial sediments are about 3 times weaker compared to the Hg vapour haloes above a flooded trench across the VMS mineralization at the Lara-Coronation occurrence (Table 2; Fig. 9). Other styles of mineralization such as pyrite-rich rocks and shear-hosted chalcopyrite-pyrite stringers have much weaker Hg vapour haloes compared to those of the polymetallic massive sulphides. Notably, elevated Hg concentrations in A- and B-horizon soils (up to 460 ppb) and vegetation (up to 133 ppb) are displaced from the sediment-covered VMS zones and cluster above the barren pyritic horizons in volcanic hosts up slope (Fig. 7; Bodnar, 2017; Heberlein et al., 2017). In contrast, the real-time Hg vapour haloes in near-surface air occur directly above the VMS zones and thus are better indicators of the buried mineralization. Shear-hosted, Hg-poor Cu-Ag-Au sulphides in mafic rocks (Sunro past-producer) at Jordan River are also marked by weak Hg vapour haloes in near-surface air (Fig. 14).

6.2. Mercury vapour haloes above faults

The terrane-bounding Leech River fault and its splay (Figs. 18, 19), thrust faults at the Lara-Coronation occurrence (Figs. 8, 9), a thrust fault at Harling Point, and other faults are marked by weak Hg vapour anomalies (1.3 to 2.2x) relative to

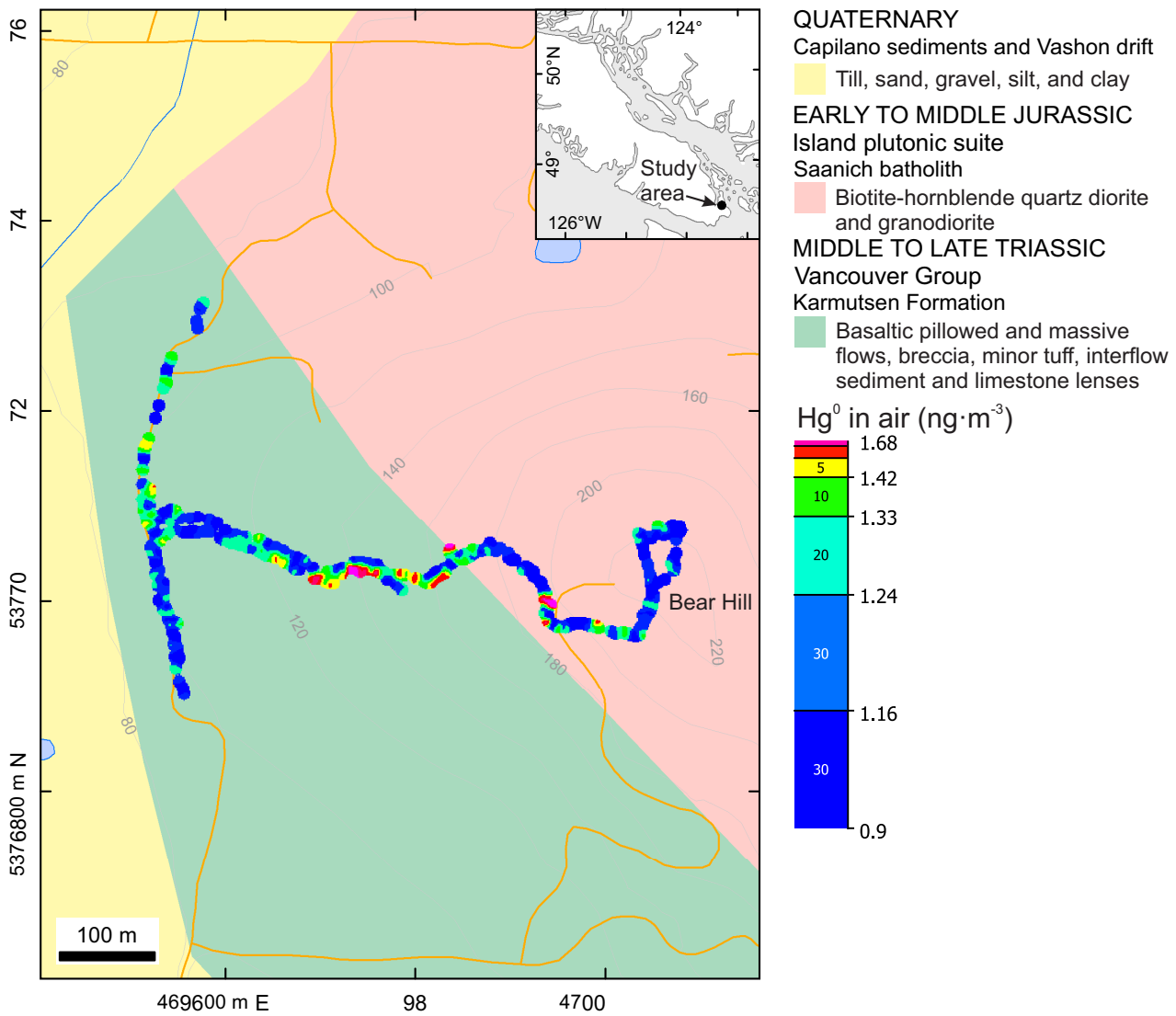


Fig. 28. Percentile-gridded, real-time Hg vapour concentrations (ng·m⁻³) in air 10-50 cm above ground at Bear Hill, central Saanich Peninsula. Gridding interpolation based on modified inverse distance weighing method. Geology after Cui et al. (2017, 2018) based on Clapp (1912, 1913), Muller (1977, 1980, 1983), and Massey et al. (1994).

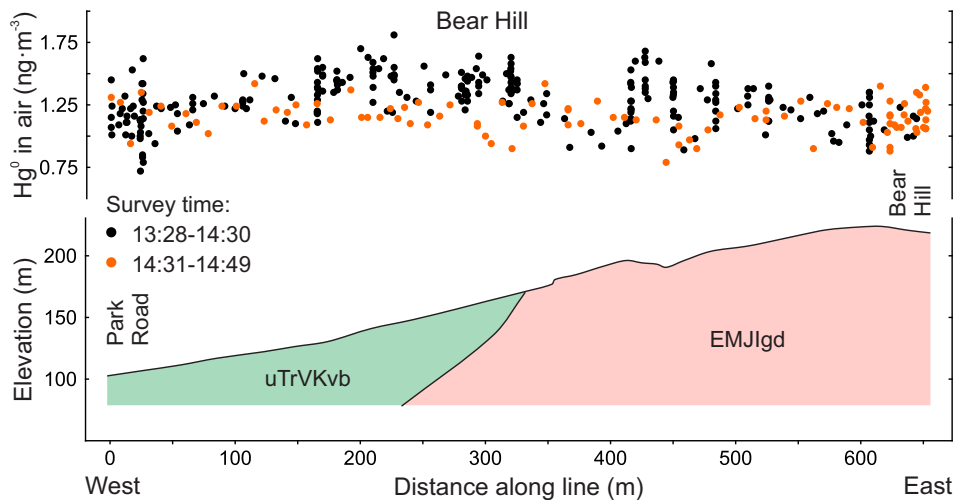


Fig. 29. Profile for Hg⁰ in air (ng·m⁻³) with respect to distance along traverse (m) and geological cross-section at Bear Hill (see Figure 28).

Table 2. Summary of Hg vapour haloes in near-surface atmosphere above mineralization and other geological features.

Location	Map sheet	Survey date	Elevation above sea level (m)	Total traverse (m)	Air sampling height above ground (cm)	Geological feature	Overburden thickness (m)	Hg ⁰ in air halo contrast
Coronation Mountain*	92B/13	06.08.2020	595 to 741	1625	10-50	Volcanogenic massive sulphide Zn-Cu-Pb-Ag-Au (Lara-Coronation)	<1	6.6
	92B/13	12.08.2020	595 to 741	3182	1-10	Fulford thrust fault	30	1.9
Mount Washington	92B/13	12.08.2020	595 to 741	3182	1-10	Volcanogenic massive sulphide Zn-Cu-Pb-Ag-Au (Lara-Coronation)	<1	4.2
	92F/14	25.08.2020	1309 to 1406	1434	10-50	Fulford thrust fault	30	1.3
Jordan River	92C/08	17.08.2020	204 to 363	1948	1-10	Porphyry Cu-Mo-Au to epithermal Au-Ag-Cu (Mount Washington Copper)	20	1.3
Goldstream	92C/08	17.08.2020	204 to 363	1948	1-10	Basalt-hosted sulphide Cu-Ag-Au in shear zones (Sunro)	<2	1.5
	92B/05	22.08.2020	37 to 121	2577	10-50	Auriferous quartz vein (Bentley Au); possibly amalgamation of ore on site	0	38.5
Skirt Mountain	92B/05	10.08.2020	62 to 257	2890	1-10	Shear-hosted sulphide Cu-Ag-Au (Ralph)	0	13.4
	92B/05	11.08.2020	109 to 166	2664	1-10	Terrane-bounding thrust fault	<2	1.8
Colwood	92B/05	11.08.2020	109 to 166	2664	1-10	Leech River thrust fault	<2	1.4
	92B/06	05.08.2020	19 to 81	2514	10-50	Splay of Leech River fault	<2	1.5
Durance Lake	92B/06	05.08.2020	19 to 81	2514	10-50	Leech River thrust fault	<10?	2.0
	92B/11	19.08.2020	134 to 197	1490	10-50	Splay of Leech River fault	<60	1.5
Elk Lake	92B/11	28.08.2020	68 to 77	766	10-50	Terrane-bounding fault	<2	2.2
	92B/11	27.08.2020	5 to 55	1759	10-50	Terrane-bounding fault	<10	1.4
Deep Cove	92B/11	27.08.2020	0 to 38	1793	1-10	Strike-slip fault	<5?	1.8
	92B/11	27.08.2020	0 to 38	1793	1-10	Granodiorite near thrust fault	<10	1.4
Bear Hill	92B/11	28.08.2020	89 to 224	1224	10-50	Intrusive contact of granodiorite pluton and mafic volcanic rocks	<1	1.5
	92B/06	08.08.2020	0 to 12	389	1-10	Terrane-bounding thrust fault	0	1.6
Victoria downtown	92B/06	25.07.2020	19 to 40	1732	10-50	Intrusive and metamorphic rocks of the Westcoast Crystalline complex	<2	1.4

Mercury vapour halo contrast is defined as a ratio of the maximum concentration of Hg⁰ in near-surface air to the background (median) Hg concentration for a given survey. *At Coronation Mountain, wet surface was still drying during the survey on August 6th, 2020, just a few hours after the end of rain in the area for several days, compared with much drier surface on August 12th, 2020 without any precipitation between the two surveys. Weather conditions were a mix of sun and clouds during both surveys.

local background (Table 2). Mercury vapour anomalies in soil gas above modern fault zones are influenced by the fault slip rate, the degree of fault fracturing, the degree of fault locking, bedrock lithology, and overburden cover (Sun et al., 2017; Xiang et al., 2020). These factors control Hg upward migration and surface enrichment. The Leech River fault has been active after the last glacial maximum ca. 17 ka (Morell et al., 2017). Mercury vapour anomalies above it and its splays indicate that these structures serve as conduits for geogenic gases, such as has been described from elsewhere by Jin et al. (1989), Stepanov (1997), Stoffers et al. (1999), Wang et al. (2006), and Xiang et al. (2020). Other faults in the Victoria area also have associated Hg anomalies, which may indicate Neotectonic activity. Elevated Hg vapour emission (1.4 to 1.5x background Hg) also occurs above the southwestern margin of the Saanich granitoid batholith at Bear Hill (Figs. 28, 29) and above felsic rocks of the Westcoast Crystalline complex in Victoria (Table 2).

6.3. Meteorological effects

Air and soil temperature, soil moisture, solar radiation, and atmospheric pressure influence the emission of Hg vapour from overburden, whereas wind and turbulent movement of air both dilute and transport gaseous Hg^0 escaping to the atmosphere (e.g., McCarthy, 1972; Gustin et al., 1997; Zhang and Lindberg, 1999; Xie et al., 2019). Although the mercury vapour concentrations in near-surface air measured in the present study generally show little effects of air temperature, relative humidity, and atmospheric pressure (Figs. 30a-c), minor variations of background Hg concentrations accompanied by

rapid changes in these parameters were noted at some locations (Appendix 1 of Rukhlov et al., 2020). Elsewhere, the mercury content of soil gas and air shows considerable diurnal as well as seasonal variations (e.g., Krömer et al., 1981; Dalziel and Tordon, 2014).

Wind speeds did have an effect in the present study (Fig. 30d). The diffusion of gaseous Hg in near-surface atmosphere is controlled by active turbulent mixing of air. Experimental and theoretical modelling of atmospheric diffusion show that wind can dilute, deform, shift, or destroy gaseous Hg haloes in near-surface atmosphere, with $4 \text{ m}\cdot\text{s}^{-1}$ being the critical speed at which a gas halo becomes unstable and turns into a plume (Mashyanov et al., 1985 and references therein). In the present study, at a wind speed of about $4.5 \text{ m}\cdot\text{s}^{-1}$, the range of measured concentrations approached the background (median) concentration of $1.40 \text{ ng}\cdot\text{m}^{-3}$ (Fig. 30d), consistent with the findings of other studies (Williston, 1968; McCarthy, 1972; Mashyanov, 1980, 1985; Gustin et al., 1999; Yasutake et al., 2011). In contrast, molecular diffusion of Hg^0 from a static source (Hg barometer) in the closed space of the British Columbia Geological Survey laboratory generated a stable Hg vapour halo, which gradually diffused to background Hg concentrations 25 metres away from the metal source.

Rain has little influence on concentrations of gaseous Hg^0 in the atmosphere, removing mainly Hg adsorbed on particulates and aerosols (Saukov, 1946; McCarthy, 1972; Mashyanov, 1985). Water bodies, bogs, snow, and permafrost do not block Hg emission into the atmosphere from underlying bedrock sources (McCarthy, 1972; Mashyanov, 1985). However, the

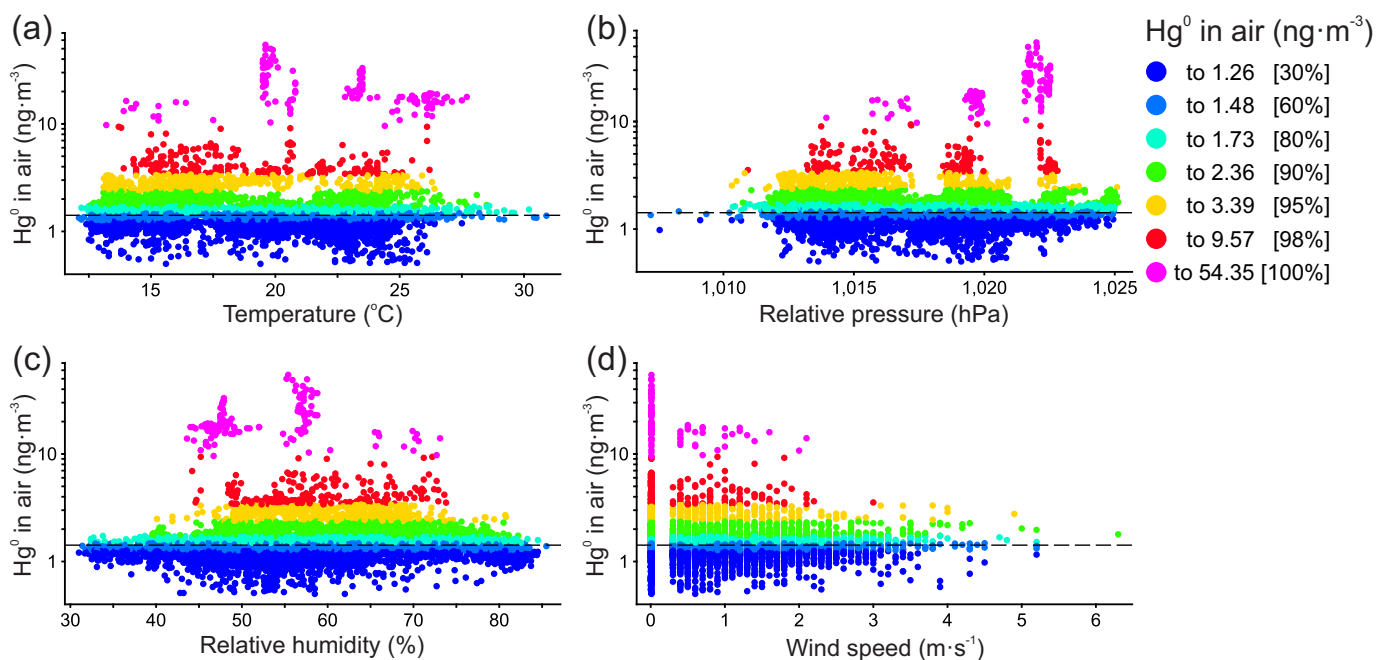


Fig. 30. Scatter plots of weather parameters vs. Hg vapour concentration in near-surface air for all data of this study. **a)** Air temperature ($^{\circ}\text{C}$) vs. Hg^0 in air ($\text{ng}\cdot\text{m}^{-3}$). **b)** Relative barometric pressure at sea-level (hPa) vs. Hg^0 in air ($\text{ng}\cdot\text{m}^{-3}$). **c)** Relative air humidity (%) vs. Hg^0 in air ($\text{ng}\cdot\text{m}^{-3}$). **d)** Wind speed ($\text{m}\cdot\text{s}^{-1}$) vs. Hg^0 in air ($\text{ng}\cdot\text{m}^{-3}$). Percentiles and median concentration of Hg^0 in air ($1.40 \text{ ng}\cdot\text{m}^{-3}$; dashed line) based on 9660 values.

effect of rapid changes in soil moisture is that as water fills pore space in soil, Hg temporarily accumulates in the top layer, adsorbing on soil particles. Subsequent heating and drying of the soil surface by solar radiation causes desorption and exhalation of Hg⁰ into the atmosphere. Depending on the type and permeability of surficial materials, rapid changes in soil moisture can increase the intensity of Hg vapour anomalies (Mashyanov, 1980, 1985; Zhrebtsov et al., 1992). The effect of soil moisture might explain the variable intensity of Hg vapour haloes at the sediment-covered Lara-Coronation polymetallic VMS occurrence (Figs. 8, 9; Table 2). Mercury anomalies in near-surface air were about 1.6x stronger when the surface was still wet a few hours after the rain, compared to the intensity of the same anomalies above the dry surface following six days without rain (Fig. 9). Weather was a mix of sun and clouds, with similar air temperature, relative humidity, and wind speed, but slightly different atmospheric pressure, during both surveys (Appendix 1 of Rukhlov et al., 2020).

7. Conclusion

We measured real-time Hg vapour concentrations 1-50 cm above ground at 15 locations that include polymetallic VMS, epithermal Au-Ag-Cu, shear-hosted sulphide Cu-Ag-Au, auriferous quartz veins, fault structures, and barren rocks on Vancouver Island. Direct and continuous (one measurement per second) monitoring of ultra-low Hg concentrations in air was made with a portable RA-915M Zeeman mercury atomic absorption analyzer. Meteorological conditions (wind speed and direction, air temperature, relative humidity, and atmospheric pressure) were simultaneously measured using a Kestrel 5500 meter. Mercury vapour concentrations (total 9660 measurements) acquired in this study range from 0.50 to 54 ng·m⁻³, with a background (median) value of 1.40 ng·m⁻³ being consistent with the global background Hg in the atmosphere. The strongest Hg emission occurs above tailings from a shaft at the Bentley Au occurrence north of Goldstream, possibly due to a mining method involving amalgamation between the late 1800s and early 1900s. Mercury vapour haloes in near-surface air (1.5 to 13.4x background Hg) mark all the mineralized zones in this study, including the Lara-Coronation polymetallic VMS buried under glacial sediments up to 30 m thick. The terrane-bounding Leech River and other faults are also highlighted by Hg vapour haloes that are 1.3 to 2.2x local background; because the Leach River fault has been active since the last glacial maximum, it is possible that some of these other faults have been as well. Wind and rapid changes in air temperature, atmospheric pressure, and soil humidity can influence the intensity of the gaseous Hg anomalies. Nonetheless, sampling of near-surface air can instantly delineate mineralized zones and faults that are buried. This simple and rapid method can be used in both regional- and property-scale exploration for ore deposits, oil and gas, geothermal zones, earthquake-hazard assessment, geological mapping, and environmental monitoring. Future detailed surveys could enhance anomaly contrasts by passive air sampling using Hg flux chambers, or by

sampling air above the disturbed, top 5-3 cm layer of surficial sediment. The mechanical disturbance of the sample site liberates Hg⁰ adsorbed onto soil particles. In addition, sampling air under a bucket by using a hose like that of Yasutake et al. (2011) would minimize the effects of atmospheric turbulence and wind.

Acknowledgments

We thank Lumex Instruments Canada for renting out a portable RA-915M Zeeman mercury atomic absorption spectrometer for this study, Patrick Sabourin (Lumex Instruments Canada) for technical support and discussions during the field season, and Raymond E. Lett (Emeritus Scientist, British Columbia Geological Survey) for guiding us to literature about early Hg studies in Canada. Neil Wildgust (British Columbia Geological Survey) provided support by accommodating a flexible Covid-19 safe field program. Bruce Northcote (British Columbia Geological Survey), Adam Larsen (Treasury Metals Inc.), Greg Kronstal (Mosaic Forest Management), and Don Steffler (Jordan River) are thanked for discussions about access and permits to enter private lands. We very much appreciate thorough reviews and constructive comments of Peter M.D. Bradshaw (Bradshaw Research Initiative for Minerals and Mining), and Lawrence B. Aspler (British Columbia Geological Survey).

References cited

- Aston, S.R., Bruty, P., Chester, R., and Riley, J.P., 1972. The distribution of mercury in North-Atlantic deep-sea sediments. *Nature* 237, 125.
- Babkin, P.V., Baranov, Yu.E., Vasiliev, V.I., Demidov, N.G., Kirikilitsa, S.I., Kuznetsov, V.A., Nikiforov, N.A., Obolenskiy, A.A., Ozerova, N.A., Smirnov, V.I., Terekhova, G.A., and Fedorchuk, V.P., 1976. Metallogeny of mercury. *Nedra, Moscow*, 255 p. (in Russian).
- Barringer, A.R., 1966. Interference-free spectrometer for high sensitivity mercury analyses of soils, rocks and air. *Bulletin of Institute of Mining and Metallurgy* 75 (714), 120-124.
- Barringer, A.R., 1969. Remote-sensing techniques for mineral discovery. In: *Proceedings of the 9th Commonwealth Mining and Metallurgical Congress, Volume 1, Institution of Mining and Metallurgy*, pp. 1-42.
- Bodnar, M.M., 2017. Modelling geochemical dispersion above a buried polymetallic volcanogenic massive sulphide deposit in a recently glaciated terrain. Unpublished M.Sc. thesis, University of British Columbia, Canada, 212 p.
- Boström K., and Fischer, D.E., 1969. Distribution of mercury in East Pacific sediments. *Geochimica et Cosmochimica Acta*, 33, 743-745.
- Bradshaw, P.M.D., 2015. Sensitive mercury spectrometers for the detection of mineral deposits, airborne mercury pollution, and underground nuclear tests. Chapter 12. In: *Barringer, Back to the Future: Airborne Geochemistry and Many Related Topics, Association of Applied Geochemists*, pp. 139-148.
- Brewer, W.M., 1918. Workings on Sunloch mine, Jordan River, Victoria Mining Division. Report of Resident Engineer, Nanaimo, B.C., British Columbia Ministry of Energy, Mines and Petroleum Resources, British Columbia Geological Survey, Property File 6031, scale 1:1200.
- Buttitta, D., Caracausi, A., Chiaraluze, L., Favara, R., and Sulli, A., 2020. Continental degassing of helium in an active tectonic setting

- (northern Italy): the role of seismicity. *Scientific Reports* 10, 162.
- Carr, R.A., Jones, M.M., and Russ, E.R., 1974. Anomalous mercury in near-bottom water of a Mid-Atlantic Rift valley. *Nature* 251, 489-490.
- Carr, R.A., Jones, M.M., Warner, T.B., Cheek, C.H., and Russ, E.R., 1975. Variation in time of mercury anomalies at the Mid-Atlantic Ridge. *Nature* 258, 588-589.
- Carr, G.R., Wilmshurst, J.R., and Ryall, W.R., 1984. Mercury as a pathfinder in exploration geochemistry-Case history studies. *Journal of Geochemical Exploration* 22, 353-354.
- Carson, D.T.J., 1960a. Geology of Mount Washington, Vancouver Island, British Columbia. Unpublished M.Sc. thesis, University of British Columbia, Canada, 116 p.
- Carson, D.T.J., 1960b. Tertiary mineral deposits of Vancouver Island. *CIM Transactions Volume LXXII*, 116-125.
- Carson, D.J.T., 1968. Metallogenic study of Vancouver Island with emphasis on the relationship of plutonic rocks and mineral deposits. Unpublished Ph.D. thesis, Carleton University, Canada, 274 p.
- Chengliang, Z., Liyin, W., Yong, D., and Shengfeng, P., 1989. Distribution of trace Hg and its mode of occurrence over Fankou Pb-Zn deposit, Guangdong, China. *Journal of Geochemical Exploration* 33, 73-83.
- Choi, H.D., and Holsen, T.M., 2009. Gaseous mercury emissions from unsterilized and sterilized soils: The effect of temperature and UV radiation. *Environmental Pollution* 157, 1673-1678.
- Clague, J.J., Fulton, R.J., and Ryder, J.M., 1982. Surficial geology, Vancouver Island and adjacent mainland, British Columbia, map. Geological Survey of Canada, Open File 837, scale 1:1,000,000.
- Clapp, C.H., 1912. Southern Vancouver Island. Geological Survey of Canada, Memoir 13, 208 p., scale 1:380,160.
- Clapp, C.H., 1913. Geology of the Victoria and Saanich map areas, Vancouver Island, British Columbia. Geological Survey of Canada, Memoir 36, 143 p., scale 1:62,500.
- Coderre, J.A., and Steinthorsson, S., 1977. Natural concentration of mercury in Iceland. *Geochimica et Cosmochimica Acta* 41, 419-424.
- Cui, Y., Hickin, A.S., Schiarizza, P., Diakow, L.J., Miller, D., Nixon, G.T., Nelson, J.L., and Ferri, F., 2018. Methods to update the digital geology of British Columbia and synopses of recently integrated mapping programs. In: *Geological Fieldwork 2017*, British Columbia Ministry of Energy, Mines and Petroleum Resources, British Columbia Geological Survey Paper 2018-1, pp. 197-215.
- Cui, Y., Miller, D., Schiarizza, P., and Diakow, L.J., 2017. British Columbia digital geology. British Columbia Ministry of Energy, Mines and Petroleum Resources, British Columbia Geological Survey Open File 2017-8, 9 p. Data version 2018-04-05.
- Dalziel, J., and Tordon, R., 2014. Gaseous mercury flux measurements from two mine tailing sites in the Seal Harbour area of Nova Scotia. *Geochemistry: Exploration, Environment, Analysis* 14, 17-24.
- Erich, E.E., and Blanchard, R., 1921. Geological map of the Jordan River area, Victoria mining district, B.C., British Columbia Ministry of Energy, Mines and Petroleum Resources, British Columbia Geological Survey, Property File 6042, scale 1:12,000.
- Esbril, J.M., Higuera, P.L., Martínez-Coronado, A., and Naharro, R., 2020. 4D dispersion of total gaseous mercury derived from a mining source: identification of criteria to assess risks related with high concentrations of atmospheric mercury. *Atmospheric Chemistry and Physics*, <https://doi.org/10.5194/acp-2019-1107>.
- Eshleman, A., Siegel, M.S., and Siegel, B.Z., 1971. Is the mercury from Hawaiian volcanoes a natural source of pollution? *Nature* 233, 471-472.
- Fedorchuk, V.P., 1964. Method of Prospecting and Exploration for Concealed Mercury-Antimony Mineralization. Nedra, Moscow, 283 p. (in Russian).
- Fedorchuk, V.P., 1983. Geology of Mercury. Nedra, Moscow, 270 p. (in Russian).
- Fridman, A.I., 1975. Gas Survey in Ore Prospecting and Geological Mapping. Institute of Mineralogy, Geochemistry and Crystal Chemistry of Rare Elements (IMGRE), Moscow, 88 p. (in Russian).
- Fursov, V.Z., 1970. Mercury atmosphere of mercury deposits. *Doklady of the Academy of Sciences of the USSR, Geology Series* 194 (6), 1421-1423. (in Russian).
- Fursov, V.Z., 1977. Mercury-Indicator for Geochemical Prospecting of Ore Deposits. Nedra, Moscow, 142 p. (in Russian).
- Fursov, V.Z., 1983a. Mercury vapour method in exploration of mineral deposits. Nauka, Moscow, 240 p. (in Russian).
- Fursov, V.Z., 1983b. Mercury in rocks and ores and its sublimation temperature. *Doklady of the Academy of Sciences of the USSR* 204 (2), 451-545. (in Russian).
- Fursov, V.Z., 1990. Mercury vapor surveys: technique and results. *Journal of Geochemical Exploration* 38, 145-155.
- Gu, B., Bian, Y., Miller, C.L., Dong, W., Jiang, X., and Liang, L., 2011. Mercury reduction and complexation by natural organic matter in anoxic environments. *Proceedings of the National Academy of Sciences of the United States of America* 108, 1479-1483.
- Guelpa, J.P., and Meusy, G., 1971. Sunro mine geological map. British Columbia Ministry of Energy, Mines and Petroleum Resources, British Columbia Geological Survey, Property File 753084, scale 1:4800.
- Gustin, M.S., Taylor, Jr., G.E., and Maxey, R.A., 1997. Effect of temperature and air movement on the flux of elemental mercury from substrate to the atmosphere. *Journal of Geophysical Research* 102, 3891-3898.
- Gworek, B., Dmuchowski, W., Baczewska, A.H., Brągoszewska, P., Bemowska-Kałabun, O., and Wrzosek-Jakubowska, J., 2017. Air contamination by mercury, emissions and transformations-a review. *Water, Air, & Soil Pollution* 228, 123.
- Hawkes, H.E., and Williston, S.H., 1962. Mercury vapour as a guide to lead-zinc-silver deposits. *The Mining Congress Journal* 48, 30-35.
- Heberlein, D.R., Dunn, C.E., and Rice, S., 2017. Halogens and other volatile compounds in surface sample media as indicators of mineralization. Part 1: Lara VMS deposit, Vancouver Island, BC (NTS 092B/13). *Geoscience BC Report 2017-11*, 43 p.
- Higuera, P., Llanos, W., García, M.E., Millán, R., and Serrano, C., 2012. Mercury vapor emissions from the Ingenios in Potosí (Bolivia). *Journal of Geochemical Exploration* 116, 1-7.
- Houle, J., 2000. Unpublished description and assay data for rock samples from Mount Washington property. British Columbia Ministry of Energy, Mines and Petroleum Resources, British Columbia Geological Survey, Property File 7223, 9 p.
- Houle, J., 2016. 2015 Technical assessment report for the New Sunro property, Vancouver Island. British Columbia. British Columbia Ministry of Energy, Mines and Petroleum Resources, British Columbia Geological Survey, Assessment Report 35982, 61 p.
- Houle, J., 2019. Technical assessment report on the Mount Washington property. British Columbia Ministry of Energy, Mines and Petroleum Resources, British Columbia Geological Survey, Assessment Report 38409, 124 p., scale 1:5000.
- Jin, Y., Wu, Z., Shen, C., Wei, J., and Zhu, H., 1989. Earthquake prediction through the observation and measurement of mercury content variation in water. *Journal of Geochemical Exploration* 33, 195-202.
- Kalinchuk, V.V., and Astakhov, A.S., 2014. Atmochemical mercury dispersion aureoles over active geologic structures of northern Japan Sea area. *Geology and Geophysics* 55, 1728-1737 (in Russian).
- Karasik, M.A., Kirilitsa, S.I., and Avgitov, A.K., 1978. Methodical Recommendations for the Interpretation of Mercury Vapour Haloes

- of Mercury Deposits in Donbass. Simferopol, 140 p. (in Russian).
- Kelso, I., and Wetherup, S., 2008. Independent technical report and mineral resource estimation: Lara polymetallic property, British Columbia, Canada. NI 43-101 Technical Report, 121 p.
- Kikauka, A., 2004. Geological and geochemical report on the Sunloch claim (Sunro copper-silver-gold mine), Jordan River, B.C., British Columbia Ministry of Energy and Mines, British Columbia Geological Survey, Assessment Report 27472, 36 p., scale 1:5000.
- Kothny, E.L., 1973. The three-phase equilibrium of mercury in nature. Chapter 4. In: Kothny, E.L. (Ed.), Trace Element in the Environment. American Chemical Society, Advances in Chemistry 123, pp. 48-80.
- Krömer, E., Friedrich, G., and Wallner, P., 1981. Mercury and mercury compounds in surface air, soil gas, soils and rocks. In: Rose, A.W. and Gundlach, H., (Eds.), Geochemical Exploration 1980. Journal of Geochemical Exploration 15, 51-62.
- Kuznetsov, V.A., and Obolenskiy, A.A., 1970. Questions of the genesis of mercury deposits and the problem of sources of ore matter. *Geology and Geophysics* 4, 44-56.
- Lett, R.E., Sacco, D.A., Elder, B., and Jackaman, W., 2020. Real-time detection of bedrock mineralization and geological faults beneath glacial deposits in central British Columbia using onsite soil gas carbon dioxide and oxygen analysis by electronic gas sensors (NTS 093A/58, 093G/03). In: Geoscience BC Summary of Activities 2019: Minerals. Geoscience BC, Report 2020-01, pp. 93-100.
- Mashyanov, N.R., 1980. Experimental development of a method of prospecting for mineral deposits using gaseous mercury aureoles in atmosphere. *Vestnik of St. Petersburg (Leningrad) State University* 12, 47-55. (in Russian).
- Mashyanov, N.R., 1985. Mercury vapour survey in near-surface layer of atmosphere for prospecting of ore deposits. Unpublished Ph.D. thesis, St. Petersburg (Leningrad) State University, St. Petersburg, 201 p. (in Russian).
- Mashyanov, N.R., 1993. Atmochemical methods in geochemistry and ecology. In: Nemets, V.M., (Ed.), Methods of Analysis of Inorganic Gases, Chemistry, St. Petersburg, pp. 340-404. (in Russian).
- Mashyanov, N.R., Ilyin, Yu.T., and Ryzhov, V.V., 1995. Electrochemical decomposition of mercury-bearing sulphides - first experimental data. In: The Universities of Russia Programme, Theme 2, Geology, Volume 2, Moscow State University, Moscow, pp. 176-180. (in Russian).
- Mashyanov, N.R., Pogarev, S.E., Panova, E.G., Panichev, N., and Ryzhov, V., 2017. Determination of mercury thermospecies in coal. *Fuel* 203, 973-980.
- Massey, N.W.D., 1995. Geology and mineral resources of the Duncan sheet, Vancouver Island, 92B/13. British Columbia Ministry of Energy, Mines and Petroleum Resources, British Columbia Geological Survey Paper 1992-4, 124 p.
- Massey, N.W.D., Friday, S.J., Tercier, P.E., and Potter, T.E., 1991. Geology of the Duncan area (92B/13). British Columbia Ministry of Energy, Mines and Petroleum Resources, British Columbia Geological Survey Geoscience Map 1991-03, scale 1:50,000.
- Massey, N.W.D., Desjardins, P.J., and Grunsky, E.C. (compilers), 1994. Vancouver Island, British Columbia, (92B, C, E, F, G, K, L; 1021). British Columbia Ministry of Energy, Mines and Petroleum Resources, British Columbia Geological Survey Open File 1994-06, scale 1:250,000.
- McCarthy, Jr., J.H., 1972. Mercury vapour and other volatile components in the air as a guide to our deposits. *Journal of Geochemical Exploration* 1, 143-162.
- McCarthy, Jr., J.H., Vaughn, W.W., Learned, R.E., and Meuschke, J.L., 1969. Mercury in soil gas and air-a potential tool in mineral exploration. U.S. Geological Survey Circular 609, 16 p.
- McCarthy, Jr., J.H., Menschke, J.L., Piclin, W.H., and Learned, R.E., 1970. Mercury in the atmosphere. In: Mercury in the Environment. U.S. Geological Survey Professional Paper 713, pp. 37-39.
- McDougall, J.J., 1987. Summary report on Mt. Washington gold property. British Columbia Ministry of Energy, Mines and Petroleum Resources, British Columbia Geological Survey, Property File 885796, 23 p.
- Meusy, G., 1971. Surface geology, Sunro Mine. British Columbia Ministry of Energy, Mines and Petroleum Resources, British Columbia Geological Survey, Property File 6056, scale 1:1200.
- Moore, C.W., and Castro, M.S., 2012. Investigation of factors affecting gaseous mercury concentrations in soils. *Science of the Total Environment* 419, 136-143.
- Morell, K.D., Regalla, C., Leonard, L.J., Amos, C., and Levson, V., 2017. Quaternary rupture of a crustal fault beneath Victoria, British Columbia, Canada. *GSA Today* 27, doi: 10.1130/GSATG291A.1.
- Muller, J.E., 1977. Geology of Vancouver Island. Geological Association of Canada, Mineralogical Association of Canada, Joint Annual Meeting 1977, Field Trip 7, April 21-24, Guidebook, 54 p.
- Muller, J.E., 1980. Geology - Victoria map area, Vancouver Island and Gulf islands, British Columbia. Geological Survey of Canada, Open File 701, scale 1:100,000.
- Muller, J.E., 1983. Geology, Victoria, west of sixth meridian, British Columbia. Geological Survey of Canada, Map 1553A, scale 1:100,000.
- Muller, J.E., 1989. Tertiary low angle faulting and related gold and copper mineralization on Mount Washington, Vancouver Island (92F/11, 14). In: Geological Fieldwork 1988, British Columbia Ministry of Energy, Mines and Petroleum Resources, British Columbia Geological Survey Paper 1989-01, pp. 81-91.
- Nelson, J.L., Colpron, M., and Israel, S., 2013. The Cordillera of British Columbia, Yukon and Alaska: tectonics and metallogeny. In: Colpron, M., Bissig, T., Rusk, B.G., and Thompson, F.H., (Eds.), Tectonics, Metallogeny, and Discovery: The North American Cordillera and Similar Accretionary Settings. Society of Economic Geologists, Special Publication 17, pp. 53-109.
- Neumann, N., 1991. The geology and history of mining at Goldstream. The Geological Association of Canada, Pacific Section, British Columbia Ministry of Energy, Mines and Petroleum Resources, British Columbia Geological Survey Property File 21792, 83 p.
- Neville, B., 1963. Mineralogy of a suite of minerals from a deposit at Mount Washington, Vancouver Island, British Columbia. Unpublished Geology 409 Course Paper, The University of British Columbia, Canada, British Columbia Ministry of Energy, Mines and Petroleum Resources, British Columbia Geological Survey, Property File 600191, 11 p.
- Nevolko, P.A., and Fominykh, P.A., 2017. Orientation mercury vapour survey at the Novolushnikovskoe gold deposit (Salair Ridge). *Razvedka i Okhrana Nedr* 6, 17-20. (in Russian).
- Northcote, K.E., and Muller, J.E., 1972. Volcanism, plutonism, and mineralization: Vancouver Island. Canadian Institute of Mining, Metallurgy and Petroleum, Bulletin 65, 49-57.
- Nriagu, J., and Becker, C., 2003. Volcanic emissions of mercury to the atmosphere: Global and regional inventories. *Science of the Total Environment* 304, 3-12.
- Ovchinnikov, L.N., Sokolov, V.A., Friedman, A.I., and Yanitakii, I.N., 1972. Gaseous geochemical methods in structural mapping and prospecting for ore deposits. In: Jones, M.J., (Ed.), Geochemical Exploration 1972, Institute of Mining and Metallurgy, pp. 177-182.
- Ozerova, N.A., 1975. Mercury in gas deposits of Central Europe. *Soviet Geology* 6, 72-79. (in Russian).
- Ozerova, N.A., 1976. Some questions on geochemistry of mercury and the problem of sources of ore matter. In: Metallogeny of Mercury. Nedra, Moscow, pp. 28-41.
- Ozerova, N.A., 1977. On degassing of mercury from depths of the Earth. In: Geochemistry of Processes of Migration of Ore Elements. Nauka, Moscow, pp. 15-35. (in Russian).

- Ozerova, N.A., 1979. On mercury contents of 'through' minerals of endogenic ore deposits. In: *Geochemical Methods of Prospecting for Polymetallic Ore Deposits*. Nauka, Novosibirsk, pp. 174-181. (in Russian).
- Ozerova, N.A., 1986. Mercury and Endogenic Ore Formation. Nauka, Moscow, 232 p. (in Russian).
- Phillips, B.A., Kerr, A.C., Mullen, E.K., and Weis, D., 2017. Oceanic mafic magmatism in the Siletz terrane, NW North America: Fragments of an Eocene oceanic plateau? *Lithos* 274-275, 291-303.
- Rehn, P., and Rehn, W., 1996. Mercury vapor anomalies at the Section 30 Deposit, Twin Creeks Mine, Nevada. In: *Geology and Ore Deposits of the American Cordillera. Proceedings of the Geological Society of Nevada Symposium, Volume 30, Reno/Sparks, Nevada*, pp. 769-778.
- Rudnick, R.L., and Gao, S., 2005. Composition of the continental crust. In: Heinrich, D.H., Rudnick, R.L., and Turekian, K.K., (Eds.), *The Crust, Treatise on Geochemistry, Volume 3*, Elsevier, Amsterdam, pp. 1-64.
- Rukhlov, A.S., Ootes, L., Hickin, A.S., and Mashyanov, N.R., 2020. Supplementary data for near-surface mercury vapour haloes in air above ore deposits and faults on Vancouver Island: Insights into buried materials in real time? *British Columbia Ministry of Energy, Mines and Low Carbon Innovation, British Columbia Geological Survey GeoFile 2020-13*, 1 p.
- Ruks, T.W., 2015. Stratigraphic and paleotectonic studies of Paleozoic Wrangellia and its contained volcanogenic massive sulfide (VMS) occurrences, Vancouver Island, British Columbia, Canada. Unpublished Ph.D. thesis, University of British Columbia, Canada, 185 p.
- Rusmore, M.E., and Cowan, D.S., 1985. Jurassic-Cretaceous rock units along the southern end of the Wrangellia terrane on Vancouver Island. *Canadian Journal of Earth Sciences* 22, 1223-1232.
- Rychagov, S.N., Nuzhdaev, A.A., and Stepanov, I.I., 2009. Behaviour of mercury in the hypergene zone of geothermal deposits (southern Kamchatka). *Geokhimiya* 5, 533-542. (in Russian).
- Ryzhov, V.V., Mashyanov, N.R., Ozerova, N.A., and Pogarev, S.E., 2003. Regular variations of the mercury concentration in natural gas. *The Science of the Total Environment* 304, 145-152.
- Saukov, A.A., 1946. Geochemistry of mercury. Academy of Sciences of the USSR, Contributions of the Institute of Geological Sciences 74, 128 p. (in Russian).
- Saukov, A.A., Aidinyan, N.K., and Ozerova, N.A., 1972. Studies of Mercury Geochemistry. Nauka, Moscow, 336 p. (in Russian).
- Schuster, E., 1991. The behavior of mercury in the soil with special emphasis on complexation and adsorption processes-A review of the literature. *Water, Air, & Soil Pollution* 56, 667-680.
- Sergeev, E.A., 1957. Methods of mercurimetric investigations. In: *Geochemical Prospecting of Ore Deposits*, Gosgeoltekhizdat, Moscow, pp. 158-165. (in Russian).
- Sholupov, S.E., and Ganeyev, A.A., 1995. Zeeman absorption spectrometry using high frequency modulated light polarization. *Spectrochimica Acta Part B: Atomic Spectroscopy* 50B, 1227-1236.
- Sholupov, S., Pogarev, S., Ryzhov, V., Mashyanov, N., and Stroganov, A., 2004. Zeeman atomic absorption spectrometer RA-915+ for direct determination of mercury in air and complex matrix samples. *Fuel Processing Technology* 85, 473-485.
- Smirnov, S.S., 1955. Oxidation zone of sulphide deposits. Academy of Sciences of the USSR, Moscow, 332 p. (in Russian).
- Sokolov, V.A., 1956. Migration of Oil and Gas. Academy of Sciences of the USSR, Moscow, 352 p. (in Russian).
- Solovov, A.P., 1985. Methods of Geochemical Exploration for Ore Deposits: Textbook. Nedra, Moscow, 294 p. (in Russian).
- Sprovieri, F., Pirrone, N., Bencardino, M., D'Amore, F., Carbone, F., Cinnirella, S., Mannarino, V., Landis, M., Ebinghaus, R., Weigelt, A., Brunke, E.-G., Labuschagne, C., Martin, L., Munthe, J., Wängberg, I., Artaxo, P., Morais, F., de Melo Jorge Barbosa, H., Brito, J., Cairns, W., Barbante, C., del Carmen Diéguez, M., Garcia, P.E., Dommergue, A., Angot, H., Magand, O., Skov, H., Horvat, M., Kotnik, J., Read, K.A., Neves, L.M., Gawlik, B.M., Sena, F., Mashyanov, N., Obolkin, V., Wip, D., Feng, X.B., Zhang, H., Fu, X., and Ramachan, R., 2016. Atmospheric mercury concentrations observed at ground-based monitoring sites globally distributed in the framework of the GMOS network. *Atmospheric Chemistry and Physics* 16, 11915-11935.
- Starr, C.C., and Frith, O.D., 1926. Report on examination of the Gabbro mine, Jordan River, B.C. British Columbia Ministry of Energy, Mines and Petroleum Resources, British Columbia Geological Survey, Property File 6051, 27 p.
- Stepanov, I.I., 1997. Mercury-indicator of "hot" hydrothermal zones and dynamic processes accompanied by deformation of rocks. Unpublished D.Sc. thesis, Institute of Mineralogy, Geochemistry and Crystal Chemistry of Rare Elements (IMGRE), Moscow, 165 p. (in Russian).
- Stevenson, W.G., 1967. Geological report on the property of Mt. Washington Copper Co. Ltd. in the Nanaimo Mining Division. British Columbia Ministry of Energy, Mines and Petroleum Resources, British Columbia Geological Survey, Property File 810035, 43 p., scale 1:6000 and 1:31,680.
- Stoffers, P., Hannington, M., Wright, I., Herzig, P., de Ronde, C., and Party, S.S., 1999. Elemental mercury at submarine hydrothermal vents in the Bay of Plenty, Taupo volcanic zone, New Zealand. *Geology* 27, 931-934.
- Sun, X., Si, X., Xiang, Y., and Liu, D., 2017. Soil mercury spatial variations in the fault zone and corresponding influence factors. *Terrestrial, Atmospheric and Oceanic Sciences* 28, 283-294.
- Sveshnikov, G.B., 1967. Electrochemical Processes on Sulphide Deposits. St. Petersburg (Leningrad) State University, St. Petersburg, 160 p. (in Russian).
- Toombs, R.B., 1951. A mineralogical study of Sunloch copper ore. Unpublished Geology 409 Course Paper, The University of British Columbia, Canada, British Columbia Ministry of Energy, Mines and Petroleum Resources, British Columbia Geological Survey, Property File 600454, 22 p.
- UN Environment, 2019. Global Mercury Assessment 2018. The United Nations Environment Programme, Economy Division, Chemicals and Health Branch, Geneva, Switzerland, 62 p. URL: <<https://www.unenvironment.org/explore-topics/chemicals-waste>>.
- Utkin, V.I., and Yurkov, A.K., 2010. Radon as a tracer of tectonic movements. *Russian Geology and Geophysics* 51, 220-227.
- Wang, G., Liu, C., Wang, J., Liu, W., and Zhang, P., 2006. The use of soil mercury and radon gas surveys to assist the detection of concealed faults in Fuzhou City, China. *Environmental Geology* 51, 83-90.
- Wetherup, S., 2010. Structural mapping and whole rock geochemical sampling: Lara polymetallic property. British Columbia Ministry of Energy, Mines and Petroleum Resources, British Columbia Geological Survey, Assessment Report 31578, 42 p., 4 appendices, scale 1:20,000.
- Williston, S.H., 1968. Mercury in the atmosphere. *Journal of Geophysical Research* 73, 7051-7057.
- Xiang, Y., Sun, X., Liu, D., Yan, L., Wang, B., and Gao, X., 2020. Spatial distribution of Rn, CO₂, Hg, and H₂ concentrations in soil gas across a thrust fault in Xinjiang, China. *Frontiers in Earth Sciences*, 8:554924. doi: 10.3389/feart.2020.554924.
- Xie, H., Liu, M., He, Y., Lin, H., Yu, C., Deng, C., and Wang, X., 2019. An experimental study of the impacts of solar radiation and temperature on mercury emission from different natural soils across China. *Environmental Monitoring and Assessment* 191, 545.
- Yasutake, A., Cheng, J.P., Kiyono, M., Uruguchi, S., Liu, X., Miura,

- K., Yasuda, Y., and Mashyanov, N.R., 2011. Rapid monitoring of mercury in air from an organic chemical factory in China using a portable mercury analyzer. *The Scientific World Journal* 11, 1630-1640.
- Yin, R., Pan, X., Deng, C., Sun, G., Yun Kwon, S., Lepa, R.F., and Hurley, J.P., 2020. Consistent trace element distribution and mercury isotopic signature between a shallow buried volcanic-hosted epithermal gold deposit and its weathered horizon. *Environmental Pollution* 259, 113954.
- Yorath, C.J., 2005. *The Geology of Southern Vancouver Island*. Harbour Publishing Co. Ltd., Madeira Park, British Columbia, 205 p.
- Zhang, H., and Lindberg, S.E., 1999. Processes influencing the emission of mercury from soils: A conceptual model. *Journal of Geophysical Research* 104, 21889-21896.
- Zherebtsov, Yu.D., Politkov, M.I., and Sikorskiy, V.Yu., 1992. *Technology of Mercurometric Prospecting of Ore Deposits*. Nedra, Moscow, 176 p. (in Russian).
- Zonghua, W., and Yangfen, J., 1981. A mercury vapor survey in an area of thick transported overburden near Shanghai, China. *Journal of Geochemical Exploration* 15, 77-92.